2017

Application of fractional calculus in modelling ballast deformation under cyclic loading

Yifei Sun
University of Wollongong, ys910@uowmail.edu.au

Buddhima Indraratna
University of Wollongong, indra@uow.edu.au

John Philip Carter
University of Newcastle

Timothy R. Marchant
University of Wollongong, tim@uow.edu.au

Sanjay Nimbalkar
University of Wollongong, sanjayn@uow.edu.au

Publication Details

Sun, Y., Indraratna, B., Carter, J. P., Marchant, T. & Nimbalkar, S. (2017). Application of fractional calculus in modelling ballast deformation under cyclic loading. Computers and Geotechnics, 82 16-30.

Application of fractional calculus in modelling ballast deformation under cyclic loading

Abstract
Most constitutive models can only simulate cumulative deformation after a limited number of cycles. However, railroad ballast usually experiences a large number of train passages that cause history-dependent long-term deformation. Fractional calculus is an efficient tool for modelling this phenomenon and therefore is incorporated into a constitutive model for predicting the cumulative deformation. The proposed model is further validated by comparing the model predictions with a series of corresponding experimental results. It is observed that the proposed model can realistically simulate the cumulative deformation of ballast from the onset of loading up to a large number of load cycles.

Keywords
calculus, fractional, application, deformation, loading, under, modelling, cyclic, ballast

Disciplines
Engineering | Science and Technology Studies

Publication Details
Sun, Y., Indraratna, B., Carter, J. P., Marchant, T. & Nimbalkar, S. (2017). Application of fractional calculus in modelling ballast deformation under cyclic loading. Computers and Geotechnics, 82 16-30.

Application of fractional calculus in modelling ballast deformation under cyclic loading

Yifei Sun, MSc (Hohai)
PhD Student, Centre for Geomechanics and Railway Engineering;
University of Wollongong, Wollongong, NSW 2522, Australia.
E-mail: ys910@uowmail.edu.au

Buddhima Indraratna, PhD (Alberta), FTSE, FIEAust, FASCE, FGS, DIC, CEng, CPEng
Distinguished Professor of Civil Engineering and Research Director
Centre for Geomechanics and Railway Engineering;
University of Wollongong, Wollongong, NSW 2522, Australia.
E-mail: indra@uow.edu.au

John P. Carter, PhD, DEng (Sydney), AM, FAA, FTSE, FIEAust, MASCE, CPEng, GAICD
Emeritus Professor, Faculty of Engineering and Built Environment;
The University of Newcastle, Callaghan NSW 2308, Australia.

Timothy Marchant, PhD (Adelaide), FAustMS
Professor of Applied Mathematics and Dean of Research,
School of Mathematics and Applied Statistics,
University of Wollongong, Wollongong, NSW 2522, Australia.

Sanjay Nimbalkar, PhD (IIT-Bombay)
Research Fellow, Centre for Geomechanics and Railway Engineering;
University of Wollongong, Wollongong, NSW 2522, Australia.

Words: 6130; Figures: 19; Tables: 2; Date of Submission: 3 September 2016
Submitted to: Computers and Geotechnics
Author for correspondence: Prof. Buddhima Indraratna,
University of Wollongong, Wollongong, NSW 2522, Australia.
Ph: +61 2 4221 3046, Fax: +61 2 4221 3293,
Email:indra@uow.edu.au

Application of fractional calculus in modelling ballast deformation under cyclic loading

ABSTRACT: Most constitutive models can only simulate cumulative deformation after a limited number of cycles. However, railroad ballast usually experiences a large number of train passages that cause history-dependent long-term deformation. Fractional calculus is an efficient tool for modelling this phenomenon and therefore is incorporated into a constitutive model for predicting the cumulative deformation. The proposed model is further validated by comparing the model predictions with a series of corresponding experimental results. It is observed that the proposed model can realistically simulate the cumulative deformation of ballast from the onset of loading up to a large number of load cycles.

KEYWORDS: Ballast; Constitutive relations; Cyclic loading; Fractional calculus

List of notations:

47	A	is the constant of proportionality
48	$\mathbf{C}^e$	is the elastic compliance matrix
49	D	means derivation
50	E	is the material constant
51	G	is the shear modulus
52	H	is the plastic modulus
53	I	means integral
54	K	is the bulk modulus
55	L	is the particle diameter
56	M	is the critical state friction parameter
57	N	is the number of load cycle
58	N_s	is the number of particles
59	R_d	is the relative density
60	b	is the fitting parameter
61	e_0	is the initial void ratio
62	f	is the load frequency
63	k	is the degradation rate of minimum sized particles
64	l_s	is the particle size
65	$\mathbf{m}$	is the plastic flow tensor
66	$\mathbf{n}$	is the loading direction tensor
67	p'	is the mean effective principal stress
68	p'_0	is the initial mean effective principal stress
69	$\overline{p}'$	is the mean effective principal stress on bounding surface
70	$\overline{p}'_0$	is the initial mean effective principal stress on bounding surface
71	p_r	is the unit pressure
72	q	is the deviator stress
73	$\overline{q}$	is the deviator stress on bounding surface
74	R	is the ratio between energy dissipation by particle rearrangement and breakage energy
75	α	is the fractional order
76	β	is the fitting parameter
77	δ_{in}	is the distance from the stress origin to the image stress point

78 δ is the distance from the current stress point to the image stress point

79 ρ is the scalar relating the image stress and the loading stress

80 η is the stress ratio between deviator stress and mean effective principal stress

81 χ is the plastic multiplier

82 λ is the gradient of the critical state line

83 κ is the gradient of the swell line

84 ν is the Poisson ratio

85 γ is the plastic flow parameter

86 γ_s is the surface shape factor

87 $\Gamma(\bullet)$ is the gamma function

88 Δ_s is the fractal dimension of the aggregates

89 $\dot{\boldsymbol{\sigma}}$ is the incremental stress tensor

90 σ_1' is the major effective principal stress

91 σ_2' is the medium effective principal stress

92 σ_3' is the minor effective principal stress

93 $\dot{\boldsymbol{\varepsilon}}$ is the incremental strain tensor

94 $\dot{\boldsymbol{\varepsilon}}^e$ is the incremental elastic strain tensor

95 $\dot{\boldsymbol{\varepsilon}}^p$ is the incremental plastic strain tensor

96 $\dot{\varepsilon}_1^p$ is the major plastic principal strain

97 $\dot{\varepsilon}_3^p$ is the minor plastic principal strain

98 ε_v^e is the elastic volumetric strain

99 ε_s^e is the generalised elastic shear strain

100 $\dot{\varepsilon}_v^p$ is the plastic volumetric strain

101 $\dot{\varepsilon}_s^p$ is the generalised plastic shear strain

102 ϕ_{cr} is the critical state friction angle

103 $\dot{S}_s$ is the incremental surface area of aggregates

104 Ω is the surface energy

105

1 INTRODUCTION

Ballast usually serves as an essential track construction layer to bear the load transmitted by railroad ties, and also to facilitate rapid drainage. During the whole operation period, a rail track usually experiences a large number of train passages that cause a cumulative deformation of the underlying ballast. Accurate prediction of the corresponding maintenance periods necessitates the development of an advanced constitutive model that captures ballast deformation and degradation. Although traditional elastoplastic constitutive models have been investigated widely and successfully applied in many fields, more effort is required to realistically describe the stress-strain relationship of ballast subjected to long term cyclic loads. Traditional plasticity approaches, including elastoplastic models [1, 2], generalised plasticity models [3, 4], and bounding surface plasticity models [5-9], are capable of incorporating cyclic loading, but often consider very limited cycles ($N < 100$). For predicting cumulative deformation under a large number of cycles ($N \geq 10^3$), these models can be inaccurate due to the inevitable accumulation of numerical errors associated with finite element analysis. There is little possibility of using these theoretical models in practical engineering where the loading usually consists of at least tens of thousands of cycles.

To overcome the above limitations, various empirical and semi-empirical models have been proposed. Although empirical models are usually problem-targeted and easy to use in engineering applications [10, 11], they do not reflect the essential mechanisms explaining aggregates degradation and related deformation. Semi-empirical models usually provide an alternative way to model cumulative deformation. For example, Suiker and de Borst [12] proposed an elasto-plastic methodology for simulating the cyclic deterioration of rail tracks by assuming that permanent deformation was caused by frictional sliding and volumetric compaction. The growth of each component of deformation was empirically simulated by a power law. François et al. [13] proposed an explicit elastoplastic model by assuming an exponential decrease of the accumulated strain. Indraratna et al. [14] proposed a pressure-dependent elasto-plastic model by introducing empirical parameters to consider the effect of particle breakage, stress ratio and number of load cycles. However, some parameters in these models require extensive and special laboratory tests and as such are often unattractive in railway problems.

Rather than selecting different modelling techniques to describe experimentally observed stress-strain behaviour, a fundamental question that arises is: are we using the correct

mathematical tools to describe material deformation? More precisely, in view of the topic of this paper, one may ask: are commonly used increments in a particular model correctly assumed as an integer order or should one choose more general operators of a fractional order? The answer to such a question is not obvious. In fact, the cumulative deformation of granular soils under cyclic loading is not only influenced by the current loading stress but also by previous loading cycles [15]. It is indeed a memory-intensive phenomenon that can be represented mathematically by using the concept of fractional calculus.

Koeller [16] developed fractional calculus for the theory of viscoelasticity to form a link between the ideal solid state, governed by Hooke's law, and the ideal liquid state, governed by Newton's law of viscosity. In the limit of an ideal solid the system has perfect memory while in the ideal liquid state it has no memory. Hence intermediate states, representing real materials, have imperfect memory and require fractional calculus to be modelled appropriately. Fractional calculus has been used successfully for problems involving soil mechanics, solid mechanics, vibration and damping.

Geotechnical applications using fractional calculus include the creep and relaxation behaviour of composite soil [17], the time dependence of Poisson's ratio [18], the strain hardening and softening behaviour of sand and clay under monotonic loading [19], the vibration of rail pads [20], and the anomalous diffusion of underground water [21, 22].

However, for the problem of interest here, the cumulative deformation of ballast subjected to a large number of load cycles, further modelling and investigation is still required. This paper aims to develop a more rigorous model for predicting the cumulative deformation of ballast subjected to a large number of loading cycles. Traditional elastoplasticity theory is used and modified by incorporating the concept of fractional calculus, and then the developed model is validated against the results of a series of laboratory test results.

2 FRACTIONAL CALCULUS

In traditional calculus the n^{th} derivative or integral of a function is defined for n taking integer values only. In fractional calculus the definitions of a derivative and an integral are generalised and n can be a non-integer. One method to generalise the definition of the repeated integral, which results in the Riemann-Liouville fractional integral of the function, $z(x)$, is given by [23]:

$$ {}_0I_x^{\alpha} z(x) = \frac{1}{\Gamma(\alpha)} \int_0^x \frac{z(\tau)\mathrm{d}\tau}{(x-\tau)^{1-\alpha}}, \quad x > 0 \tag{1} $$

where I signifies an integral. α is the fractional order, ranging from 0 to 1, which can be correlated to the fractal dimension of a given granular material, as indicated in the Appendix. x denotes the independent variable. In this context, x can be regarded as the loading time in a static load test or the number of loading cycles in a cyclic load test. The conventional gamma function $\Gamma(x)$ is defined as:

$$ \Gamma(x) = \int_0^{\infty} e^{-\tau} \tau^{x-1} d\tau \tag{2a} $$

and obeys the recurrence relationship:

$$ \Gamma(x+1) = x\Gamma(x) = x! \tag{2b} $$

The Riemann-Liouville fractional derivative of the function $z(x)$ can be formulated as [23]:

$$ {}_0D_x^{\alpha} z(x) = \frac{d^{\alpha} z(x)}{dx^{\alpha}} = \frac{1}{\Gamma(1-\alpha)} \frac{d}{dx} \int_0^x \frac{z(\tau) d\tau}{(x-\tau)^{\alpha}}, \quad x > 0 \tag{3} $$

where D means derivation. Clearly, the fractional derivative is defined on an interval and this is contrary to the integer order differential operators defined at a single point. In other words, the value of the fractional order derivative of the function z depends not just on the value of z at x, but over the stipulated range from 0 to x. Due to its integral definition of the derivative, a fractional order derivative inherently has a strong memory, associated with the variable x. Such memory is absent from the traditional integer order derivative.

3 FRACTIONAL STRAIN ACCUMULATION RATE FOR BALLAST

In the model presented here, ballast is assumed to be homogeneous and isotropic, compression is considered to be positive, and tension as negative. Triaxial stress notations are used in this formulation.

Many constitutive models concerned with the stress-strain behaviour of granular materials under triaxial loading have been proposed, e.g., [24-26]. By regarding a granular soil as an

intermediate material lying between 'ideal' solids (e.g., steel, concrete) which obey Hooke' law of elasticity, and Newtonian fluids (e.g., water, lubricant oil) which satisfy Newton's law of viscosity, Yin et al. [19] proposed a general framework for fractional order constitutive modelling of soils under static loading. For clarification, their work is briefly introduced here. The basic constitutive law of an intermediate material can be defined as:

$$\sigma = E\theta^{\alpha}{}_{0}D_{t}^{\alpha}\varepsilon, \qquad 0 \le \alpha \le 1 \tag{4}$$

where σ and ε are stress and strain, respectively, and E and θ are material constants. Note that Hooke's law with $\alpha = 0$ (the perfect memory case) and Newton's law with $\alpha = 1$ (the no memory case) are just special cases of Eq. (4), which was demonstrated to be efficient and simple in modelling the static behaviour of geomaterials [19, 27]. However, the fractional order models available to date for soils, including Eq. (4), are all phenomenological models that use viscoelasticity to simulate the stress-strain response of soils. Therefore, a fractional order elastoplastic model, which possesses the advantages of both the fractional order (and hence partial memory) and irrecoverable straining of the elastoplastic approaches for geomaterials, should be proposed. In fact, the cyclic behaviour of ballast is a history-dependent phenomenon where the current deformation of ballast is often influenced by its previous loading history [14]. The fractional derivative of a variable, as shown in Eq. (3), is not only determined by the state of the current differentiation point, but also by its performance during the whole loading period, from 0 to *x*. The start of loading (first cycle, *N* = 1) simulates the first train passage. As will be demonstrated, use of the fractional rate for strain accumulation is an alternative way to model the cumulative deformation of the ballast under repeated cycles of loading.

The type of ballast used in this study was a typical angular/sub-angular volcanic latite basalt that contains the primary minerals feldspar, plagioclase, and augite [28]. The material properties (grading, void ratio, etc.) and the relevant test conditions are given in Table 1. Note that for all cases listed in this table the test ID symbol refers to the test condition, e.g., S100 indicates a static test (S) under a confining pressure of 100 kPa, and C30f20 indicates a cyclic test (C) under a confining pressure of 30 kPa and a load frequency (*f*) of 20 Hz. Aggregates selected from each size range were carefully washed, air-dried, and then weighed separately and mixed together before being placed into a large-scale triaxial specimen with a height = 600 mm and a diameter = 300 mm. The maximum and minimum void ratios were tested to be 0.96 and 0.61, respectively [29]. The specimens were isotropically compressed at

an effective confining pressure of 30 kPa before an axial load was applied. Cyclic tests were conducted with an input maximum deviator stress q_{max} of 230 kPa and a minimum deviator stress q_{min} of 45 kPa. A typical harmonic cyclic load (sinusoidal waveform) was used during the cyclic loading tests at a frequency equal to 20 Hz. Membrane correction was applied to the current test results according to ASTM 2011 [30]. In the context of cyclic load testing, the number of load cycles *N*, instead of the time *t*, is used [13, 31] as a measure of the cumulative strain rate during cyclic loading ($d\varepsilon/dN$). Fig. 1(a) shows the variations in the axial strain accumulation rate with the number of load cycles. It is observed that the strain accumulation rate initially decreased markedly, and then stabilised as the number of load cycles increased. However, by replotting the strain accumulation rate and the number of load cycles on *log-log* scales, a simple linear variation can be observed, as shown in Fig. 1(b). Fig. 2 shows a similar phenomenon where a simple linear variation between the volumetric strain rate and the number of load cycles can be expected. For test conducted under low confining pressure, the axial compression (+) along with radial expansion (-) was observed and the overall volumetric strain was smaller than that observed under relatively high confining pressure (i.e., both axial and radial strains were +). However, with the progressive development of load cycles, the sample approaches shakedown. During this period, samples tested under low confining pressure experience a higher strain rate than that observed under relatively high confining pressure. Therefore, some intersection of the fitted curves is inevitable. Similar observations can be found in [32]. Hence, the strain accumulation rate $\dot{\varepsilon}^p$, with respect to the number of load cycles *N* can be considered as scale invariant, obeying a power law in relation to the number of load cycles. This behaviour can be described by the following fractional rate for strain accumulation:

$$ {}_1D_N^{\alpha}\varepsilon^p = b\Gamma(\alpha) \tag{5}$$

where the term *D* indicates derivation as defined in Eq. (3). ε^p denotes, in general, the plastic strain. The fractional derivative order is $\alpha = 1-\beta$, in which β and *b* are fitting parameters, as shown in Figs 1(b) and 2(b). They remain constant for a specific loading state applied for each triaxial test (i.e., for a given confining pressure, load amplitude and load frequency). As demonstrated later, the parameter *b* is more likely to depend on the triaxial stress state, such as the mean effective principal stress p' and the deviator stress *q*. Similar phenomena can also be observed in Fig. 3 where a different ballast [33] with two distinct particle sizes (Table 1) was tested under a load frequency of 1 Hz. A constant strain accumulation rate can

therefore be suggested if a fractional scale for differentiation with respect to the number of load cycles is used.

4 CONSTITUTIVE MODEL INCORPORATING FRACTIONAL CALCULUS

The traditional bounding surface plasticity theory is modified in this section using the fractional rate of strain accumulation with increasing number of load cycles. The total increments of strain $\dot{\boldsymbol{\varepsilon}}$, can be decomposed into the incremental plastic strain $\dot{\boldsymbol{\varepsilon}}^p$, and the elastic strain increment $\dot{\boldsymbol{\varepsilon}}^e$, respectively.

$$\dot{\boldsymbol{\varepsilon}} = \dot{\boldsymbol{\varepsilon}}^e + \dot{\boldsymbol{\varepsilon}}^p \tag{6}$$

Following the traditional elasticity theory, the incremental elastic strain can be expressed as:

$$\dot{\boldsymbol{\varepsilon}}^e = \mathbf{C}^e \dot{\boldsymbol{\sigma}} \tag{7}$$

where the elastic strain tensor $\boldsymbol{\varepsilon}^e = \left[\varepsilon_v^e, \varepsilon_s^e\right]^T$, The plastic volumetric strain $\varepsilon_v^p = \varepsilon_1^p + 2\varepsilon_3^p$ and the generalised plastic shear strain $\varepsilon_s^p = 2\left(\varepsilon_1^p - \varepsilon_3^p\right)/3$. ε_1^p and ε_3^p are the major and minor principal plastic strains, respectively. The stress tensor $\boldsymbol{\sigma} = \left[p', q\right]^T$ where the mean effective principal stress $p' = \left(\sigma_1' + 2\sigma_3'\right)/3$ and the deviator stress $q = \sigma_1' - \sigma_3'$. σ_1' and σ_3' are the major and minor effective principal stresses, respectively. $\mathbf{C}^e$ is the isotropic elastic compliance matrix, defined as:

$$\mathbf{C}^e = \begin{bmatrix} \dfrac{1}{K} & \\ & \dfrac{1}{3G} \end{bmatrix} \tag{8}$$

where the bulk modulus $K = (1+e)/\kappa p'$, and the shear modulus $G = 3(1-2\nu)/2/(1+\nu)K$. e and ν are the void ratio and Poisson's ratio, respectively. As demonstrated previously, the accumulated strain can be better described by using a fractional order derivative. So, instead of using the traditional incremental definition of the strain accumulation rate [14], the incremental plastic strain, $\dot{\boldsymbol{\varepsilon}}^p$, can be fractionally defined as:

281 $$ {}_1D_N^{\alpha}\boldsymbol{\varepsilon}^p = \chi\frac{\partial g}{\partial \boldsymbol{\sigma}} \tag{9} $$

282 where χ is the plastic multiplier and g is the plastic potential function. By recalling Eq. (5),
283 $\chi\partial g/\partial\boldsymbol{\sigma}$ should remain constant in the fractional scale for a given loading state. Therefore,
284 by applying the derivation of order $1-\alpha$ to both sides of Eq. (9), one can obtain:

285 $$ \dot{\boldsymbol{\varepsilon}}^p = \chi\frac{\partial g}{\partial \boldsymbol{\sigma}}\frac{N^{\alpha-1}}{\Gamma(\alpha)} \tag{10} $$

286 As can be seen from Eq. (10), the plastic deformation is now determined by the applied stress,
287 the gradient of the plastic potential, $\partial g/\partial\boldsymbol{\sigma}$, and the number of loading cycles, N . In
288 numerical computation of Eq. (10), $N = i$ is used during the integration of i-th number of
289 loading cycle, owing to the scale invariance of $\dot{\boldsymbol{\varepsilon}}^p$ with respect to N. The accumulated strain
290 in one loading cycle is then computed by adding up the strain increment of each sub-loading
291 step.

292

293 4.1 LOADING SURFACE AND BOUNDING SURFACE

294 Traditional bounding surface plasticity theory is a framework for the constitutive
295 modelling of granular soils, including ballast [9] and rockfill [8]. This theory consists of three
296 essential components, i.e., the loading surface, the bounding surface, and the hardening rule.
297 For the sake of simplicity, the following Cam-clay loading surface [34] is used:

298 $$ g = q - Mp'\left[\ln(p_0'/p')\right] = 0 \tag{11} $$

299 where M $(=6\sin\phi_{cr}/(3-\sin\phi_{cr}))$ is related to the critical state friction angle ϕ_{cr}. p_0' defines
300 the size of the loading surface and represents the intercept of the abscissa with the p' axis. It
301 should be noted that the use of the Cam-clay model instead of the Granta Gravel model [34]
302 is because the Granta Gravel model has assumed that the material would be totally rigid and
303 would have no recoverable strain, which is not appropriate for ballast. The shape of Cam-clay
304 bounding surface when intersecting the p' axis should be perpendicular to it to ensure the
305 correct material yielding response subjected to isotropic compression. However, field ballast
306 is usually loaded under shearing stress where the overall shape of the yield surface is
307 compatible with this stress range (45 kPa – 230 kPa). Moreover, in general plasticity

modelling, the form of loading surface has been adjusted from the conventional norm due to various loading conditions without adversely affecting the accuracy of the strain calculations. How this classical yield surface (albeit not perpendicular to p' axis) is adopted to determine the appropriate strains under a given stress combination is described in detail by Schofield and Wroth [34]. For instance, the Cam-clay model has been successfully used and modified in various past studies to describe the constitutive behaviour of sand [35, 36], ballast [37, 38] and coarser rockfill [8]. The bounding surface is usually assumed to have the same shape as the loading surface:

$$f = \overline{q} - M\overline{p}'\left[\ln(\overline{p}_0'/\overline{p}')\right] = 0 \tag{12}$$

where $\overline{p}_0'$ denotes the size of the current bounding surface. The Cam-clay bounding surface is used in this study because the constitutive model equations and the calculation of bounding surface plasticity [39] does not specify any particular form of the loading and bounding surfaces. The Cam-clay surface is simple but can still reasonably address the stress-strain behaviour of ballast if an appropriate flow rule and a hardening modulus are to be used The image stress point on the bounding surface can be then expressed by the radial mapping rule [40] using a scalar ρ as [7]:

$$\overline{p}' = \rho\overline{p}_0' \tag{13a}$$

$$\overline{q} = \rho\eta\overline{p}_0' \tag{13b}$$

where the stress ratio η is defined as follows:

$$\eta = \frac{q}{p'} = \frac{\overline{q}}{\overline{p}'} \tag{14}$$

By substituting Eqs (13) and (14) into Eq. (12), the scalar ρ which determines the image stress point on the bounding surface can be given as:

$$\rho = \exp\left[-\left(\frac{\eta}{M}\right)\right] \tag{15}$$

The position of the initial bounding surface ($\overline{p}_{0i}'$) can be determined by intersecting the normal compression line and the swelling line at point (e_0, p_{ic}'), as shown in Fig. 4:

$$\overline{p}_{0i}' = p_r \exp\left[\frac{e_\Gamma - e_0 - \kappa \ln p_{ic}'}{\lambda - \kappa} + 1\right] \tag{16}$$

where e_0 denotes the initial void ratio prior to shearing. p_r is the unit pressure. λ and κ are gradients of the critical state and swelling lines, respectively. e_Γ is the void ratio at $p' = 1$.

4.2 LOADING DIRECTION AND PLASTIC FLOW DIRECTION

The loading direction is normal to the bounding surface and can be expressed as:

$$\mathbf{n} = \left[n_{fv}, n_{fs}\right]^T \tag{17}$$

where the compression-related component is given by:

$$n_{fv} = \frac{\dfrac{\partial f}{\partial \overline{p}'}}{\left\|\dfrac{\partial f}{\partial \overline{\boldsymbol{\sigma}}}\right\|} = \frac{1}{\overline{p}'}\left[1 - \left(\frac{\eta}{M}\right)\right]\left\|\frac{\partial f}{\partial \overline{\boldsymbol{\sigma}}}\right\|^{-1} \tag{18a}$$

and the shear-related component by:

$$n_{fs} = \frac{\dfrac{\partial f}{\partial \overline{q}}}{\left\|\dfrac{\partial f}{\partial \overline{\boldsymbol{\sigma}}}\right\|} = \frac{1}{\overline{p}'}\left\|\frac{\partial f}{\partial \overline{\boldsymbol{\sigma}}}\right\|^{-1} \tag{18b}$$

In the above equations, the gradient amplitude is given by:

$$\left\|\frac{\partial f}{\partial \overline{\boldsymbol{\sigma}}}\right\| = \frac{1}{\overline{p}'}\sqrt{\left[1 - \left(\frac{\eta}{M}\right)\right]^2 + 1} \tag{19}$$

For ballast, a non-associated flow rule is used. By recalling Eq. (10), one has:

$$d_g = \frac{\dot{\varepsilon}_v^p}{\dot{\varepsilon}_s^p} = {}_0D_N^{1-\alpha}\left[\chi \frac{\partial g}{\partial p'}\right] \Big/ {}_0D_N^{1-\alpha}\left[\gamma\chi \frac{\partial g}{\partial q}\right] = (M - \eta)/\gamma \tag{20}$$

The equation above can be regarded as the cyclic flow rule for the ballast material. γ is a material constant. Accordingly, the flow direction can be defined as:

$$\mathbf{m} = \left[m_{gv}, m_{gs}\right]^T = \left[\frac{d_g}{\sqrt{1 + d_g^2}}, \frac{1}{\sqrt{1 + d_g^2}}\right]^T \tag{21}$$

352 4.3 HARDENING RULE

353 In bounding surface plasticity, the hardening modulus H is related to both the size of the
354 bounding surface and the distance between the current loading and bounding surfaces.
355 Therefore, it can be conveniently decomposed into two components [7]:

356 $$H = H_b + H_\delta \tag{22}$$

357 where H_b is the plastic modulus at $\bar{\boldsymbol{\sigma}}$ on the bounding surface, and H_δ is related to the
358 distance between the current loading surface and the bounding surface. By applying the
359 consistency condition at the bounding surface (Eq. (12)) and assuming isotropic hardening of
360 the bounding surface with plastic volumetric compression, the derivatives of the bounding
361 surface can be obtained as:

362 $$\frac{\partial f}{\partial \bar{p}'}\dot{\bar{p}}' + \frac{\partial f}{\partial \bar{q}}\dot{\bar{q}} + \frac{\partial f}{\partial \bar{p}_0'}\frac{\partial \bar{p}_0'}{\partial \varepsilon_v^p}\dot{\varepsilon}_v^p = 0 \tag{23}$$

363 By recalling Eq. (10), the plastic volumetric strain $\dot{\varepsilon}_v^p$ can be rewritten as:

364 $$\dot{\varepsilon}_v^p = \frac{\partial g}{\partial p'}\frac{\chi}{\Gamma(\alpha)}N^{\alpha-1} \tag{24}$$

365 Substituting Eq. (24) into Eq. (23) and using the definition of the unit vector normal to the
366 bounding surface, the hardening modulus H_b, can now be derived as:

367 $$H_b = -\frac{\partial f}{\partial \bar{p}_0'}\frac{\partial \bar{p}_0'}{\partial \varepsilon_v^p}\frac{m_{gv}}{\left\|\frac{\partial f}{\partial \bar{\boldsymbol{\sigma}}}\right\|}\frac{N^{\alpha-1}}{\Gamma(\alpha)} \tag{25}$$

368 where the relationship between p_0' and ε_v^p under isotropic loading can be formulated by
369 using the fractional rate for volumetric strain accumulation. Hence:

370 $$\frac{\partial \bar{p}_0'}{\partial \varepsilon_v^p} = \frac{(1+e_0)}{\lambda-\kappa}\bar{p}_0' N^{1-\alpha} \tag{26}$$

371 Note that Eq. (26) reduces to the virgin loading condition for N = 1. The cumulative
372 volumetric strain decreases with increasing load cycles, indicating a state of cyclic
373 densification of the ballast. A distinct effect of the fractional derivative order on the plastic
374 modulus can be observed from Eq. (26), where the plastic modulus H_b, decreases with the
375 decreasing order of the fractional derivative, indicating that more plastic strain is

accumulated during the cyclic loading. Similar to Russell and Khalili [41], the hardening modulus component H_δ can be given as:

$$H_\delta = h_0 p' \frac{1+e_0}{\lambda-\kappa}\frac{\delta}{\delta_{in}-\delta} \tag{27}$$

where h_0 is a material parameter that can be defined as a function of the initial conditions [42] or changing state [8, 40], for general application. For cyclic triaxial tests under different loading frequencies (f) or effective confining pressures (σ_3'), the following generalisation of h_0 can be given:

$$h_0 = a(Ty)^c \tag{28a}$$

where a and c are material constants and $Ty = f$ (or σ_3', or σ^{ampl}), corresponding to tests under different load frequencies, f, (or confining pressures, σ_3', or load amplitudes, σ^{ampl}). δ_{in} and δ are the distances from the stress origin and current stress point to the image stress point, respectively. Following the radial mapping rule [40], it is easy to obtain:

$$\frac{\delta}{\delta_{in}-\delta} = \frac{\bar{p}_0' - p_0'}{p_0'} \tag{28b}$$

The hardening modulus H approaches H_b with an increasing loading stress and ultimately equals H_b when the loading surface coincides with the bounding surface. H_δ approaches infinity if $\delta_{in}-\delta \to 0$, implying a state of no plastic deformation. By combining Eqs (10), (17), (21), and (22), a fractional order constitutive relationship between the incremental plastic strain and stress can be determined as:

$$\dot{\boldsymbol{\varepsilon}}^p = \frac{1}{H}\mathbf{n}^T\dot{\boldsymbol{\sigma}}\mathbf{m}\frac{N^{\alpha-1}}{\Gamma(\alpha)} \tag{29}$$

Eq. (29) is different from the traditional elasto-plastic model as it considers the number of load cycles by incorporating the concept of fractional calculus. By substituting Eqs (6) and (29) into Eq. (7), the generalised constitutive equation can be obtained as:

$$\dot{\boldsymbol{\varepsilon}} = \left(\mathbf{C}^e + \frac{1}{H}\frac{N^{\alpha-1}}{\Gamma(\alpha)}\mathbf{m}\mathbf{n}^T\right)\dot{\boldsymbol{\sigma}} \tag{30}$$

The above formulation incorporates fractional calculus into traditional plasticity theory. Semi-empirical elasto-plastic formulae with $\alpha = 1/3$ proposed by Liu and Carter [2] and Indraratna et al. [14] are special cases that can be derived theoretically from the proposed approach. Eq. (30) simplifies to the traditional monotonic constitutive formulae for granular soils with $\alpha = 1$. A flow chart showing how to implement the proposed model in prediction of cumulative deformation of ballast can be found in Fig. 5. As Fig. 6 shows, the proposed model predicts the equivalent stress-strain behaviour for virgin loading and first unloading. However, the fractional order greatly affects the subsequent densification of soils as shown in Fig. 6(a). The repeated shear straining causes faster densification with decreasing values of the fractional order α (from 0.65 to 0.35). For instance, the strain accumulation rate decreases from 0.61% to 0.24% at N = 10 and from 0.12% to 0.03% at N = 100, as can be observed in Fig. 6(b). The rate of cyclic densification can be simulated appropriately by an appropriate choice of the value of the fractional order, α.

5 MODEL VALIDATION

5.1 IDENTIFICATION OF MODEL PARAMETERS

The proposed model requires 9 parameters to completely characterise the cumulative behaviour of ballast subjected to monotonic and cyclic loading. Two parameters κ and ν, define the elastic behaviour. κ can be determined by measuring the slope of the swelling line in an isotropic compression test in $e - \ln p'$ space. Poisson's ratio ν, is taken as 0.3 for the ballast investigated in this study. There are three critical state parameters ϕ_{cr}, λ, and e_Γ. The critical state friction angle ϕ_{cr}, can be determined by fitting the critical state stress points in the $p' - q$ plane. Parameters λ and e_Γ, can be determined by fitting a straight line to the critical state points in the $e - \ln p'$ space. λ denotes the gradient of the critical state line and e_Γ is the intersection of the critical state line with the $p' = 1$ line. The hardening parameters a and c determine the value of h_0 and can be obtained by fitting the stress-strain curve in $q - \varepsilon_s$ space. Parameter γ controls the direction of plastic flow and can therefore be determined by simulating the stress dilatancy relationship as indicated by Fu et al. [43]. One additional parameter that is different from traditional plasticity theory is the fractional order α, for strain accumulation. It can be determined by trial and error to provide the best description of

429 the ballast densification. All parameters used in this study are listed in Table 2 (Note: $\alpha = 1$
430 for monotonic loading). As the flow direction changes [31], different values of γ are selected
431 for monotonic and cyclic loading conditions for the purpose of more realistic modelling. A
432 similar approach can be found in Khalili et al. [5, 44] and Suiker and de Borst [12].

433

434 5.2 MODEL PERFORMANCE

435 The ability of the proposed model to predict cumulative deformation of typical rail ballast
436 under monotonic and cyclic loading is investigated by comparing the numerical predictions
437 of the model and experimental results obtained from the current study and other available
438 information [14, 32, 37, 45, 46]. For all cases examined here, details of the experimental tests
439 and the ballast materials tested are provided in Table 1, and values of the model parameters
440 assumed for each ballast type in the numerical predictions are listed in Table 2.

441 Figs 7 - 10 show the results of the experimental and simulated monotonic and cyclic tests
442 carried out on a ballast ('Current study' in Table 1) under different confining pressures and
443 densities. The initial conditions for three different medium dense samples (relative density, R_d
444 = 0.56 – 0.63) tested under monotonic loads are: (i) $p' = 100$kPa and e_0 = 0.735; (ii)
445 $p' = 200$kPa and e_0 = 0.728; (iii) $p' = 400$kPa and e_0 = 0.711. The purpose of conducting
446 the monotonic tests at different confining pressures was to obtain the critical state parameters
447 for cyclic simulation. To allow the samples at least to approach the critical state at the end of
448 the test, relatively large confining pressures were used. The monotonic simulations (Fig. 7)
449 show that the model captures well the characteristic features, such as strain hardening, stress
450 dilation, and contraction of the medium dense ballast under different confining pressures. The
451 peak stresses are predicted higher than the experimental results but the volumetric strains
452 under different confining pressures are well matched. The initial conditions for samples
453 tested under cyclic loads are: $p' = 30$kPa and e_0 = 0.713; $p' = 60$kPa and e_0 = 0.708;
454 $p' = 120$kPa and e_0 = 0.671. Some models can only simulate accumulated strain accurately
455 for a limited number of cycles and fail to predict deformation accurately at large numbers of
456 load cycles ($N \geq 10^3$), while others can only give a reasonable prediction of deformation
457 under a large number of load cycles but fail to address deformation adequately at low cycle
458 numbers ($N < 100$). For example, as shown in Fig. 8, the original bounding surface model
459 with $\alpha = 1$ in this study can reasonably simulate the cumulative deformation of ballast within

460 10 load cycles, but it fails to predict the ballast deformation beyond $N > 10$. This is because
461 the hardening behaviour was not addressed properly in the original bounding surface model
462 where the model hardened gradually. However, if the fractional order is incorporated, the
463 speed of material hardening can be controlled by using an appropriate value of α. As can be
464 observed, the proposed model can capture well the axial and volumetric strains from the
465 beginning of the cyclic loading up to 50,000 cycles. The predicted axial and volumetric
466 strains are observed to increase rapidly in the initial loading stage and then gradually
467 stabilises as the number of load cycles is increased, and good agreement is found with the
468 experimental results. The fractional order α = 0.5 provides an accurate description of the
469 cyclic densification of ballast under different confining pressures. The difference in
470 prediction between the original and modified bounding surface models can be attributed to
471 the different hardening speed, as illustrated in Eq. (26). With a reduction in the fractional
472 order α, the model hardens more rapidly.

473 The initial conditions for three different dense samples (R_d = 0.70 – 0.89) tested under
474 monotonic loads are: (i) $p' = 100$kPa and e_0 = 0.686; (ii) $p' = 200$kPa and e_0 = 0.653; (iii)
475 $p' = 400$kPa and e_0 = 0.620. The monotonic simulations shown in Fig. 9 reveal that the
476 proposed model can also capture the stress-strain behaviour of the dense ballast under
477 varying confining pressures. Both the evolutions of deviator stresses and volumetric strains
478 are well simulated. The initial conditions for samples tested under cyclic loads are:
479 $p' = 30$kPa and e_0 = 0.688; $p' = 60$kPa and e_0 = 0.655; $p' = 120$kPa and e_0 = 0.623.
480 However, as Fig. 10 shows, the proposed model can also capture well the axial and
481 volumetric strains of the dense ballast samples from the beginning of the cyclic loading up to
482 50,000 cycles. A more rapid increase of the predicted axial and volumetric strains is observed
483 at the initial loading stage and then both gradually stabilise as the number of load cycles
484 increases, and this is in good agreement with the corresponding experimental results.

485 Figs 11-12 show the simulation results for monotonic and cyclic tests conducted by Salim
486 and Indraratna [37] and Indraratna et al. [14] on ballast under different loading conditions.
487 Monotonic tests were carried out on the specimens 300 mm in diameter and 600 mm high,
488 under confining pressures of 100 kPa, 200 kPa, and 300 kPa. Detailed physical properties and
489 the test conditions for each sample are listed in Table 1. Fig. 11 shows comparisons between
490 the test results and model simulations of the stress-strain response of ballast under different
491 confining pressures. It is observed that the proposed model can capture well the stress-strain

response of ballast, especially its stress dilation behaviour under a relatively low confining pressure of 100 kPa. It can also characterise the strain hardening and volumetric contraction of ballast under relatively high pressures of 200 kPa and 300 kPa. The cyclic tests were carried out at a constant confining pressure of 60 kPa and three different loading frequencies, 10 Hz, 20 Hz, and 40 Hz. A sinusoidal stress wave with a minimum deviator stress equal to 45 kPa and a maximum stress equal to 230kPa was applied during the cyclic loading period. An accurate description of cyclic densification can be obtained for this ballast material using $\alpha = 0.55$. As Fig. 12 shows, as the number of loading cycles increases permanent deformation also increases rapidly and then approaches a stable value, which can be characterised well by the fractional order plasticity model.

Fig. 13 shows the model simulations of cumulative axial and volumetric strains of another ballast material under a loading frequency of 10 Hz and two different confining pressures of 30 kPa and 60 kPa. The ballast studied in this case had a coefficient of uniformity of 1.5 and was compacted to have an initial void ratio e_0 of around 0.72 [46]. As can be observed, with the increase of the confining pressure, axial strain increased while volumetric strain decreased due to the larger radial expansion under lower confinement. These results are well captured by the fractional order model with $\alpha = 0.53$.

Figs 14 and 15 show the simulation results for monotonic and cyclic tests conducted by Anderson and Fair [45]. The monotonic tests were carried out on cylindrical specimens with a nominal height of 455 mm and a nominal diameter of 236 mm, under confining pressures equal to 40 kPa and 90 kPa. Fig. 14 shows a comparison between the monotonic test results and the corresponding model predictions where good agreement can be observed. Cyclic tests were carried out on samples with two different confining pressures and a fixed loading frequency of 0.5 Hz, as indicated in Table 1. Fig. 15 shows the simulation results of the corresponding experimental data. As can be expected, with the increase in confining pressure, the cumulative axial strain decreases while the cumulative volumetric strain increases. The proposed model can accurately simulate such an evolutionary trend when $\alpha = 0.48$.

Figs 16 and 17 show the simulation results for monotonic and cyclic tests conducted by Aursudkij et al. [32]. Monotonic tests were carried out on cylindrical specimens with a height of 450 mm and a diameter of 300 mm under confining pressures of 10 kPa, 30 kPa, and 60 kPa. Fig. 16 presents the model predictions of the corresponding test results. It is observed that the proposed model can capture well the stress-strain response of ballast, especially the

stress-dilation behaviour at low confining pressures (≤ 60 kPa). Cyclic tests were carried out at confining pressures of 30 kPa and 60 kPa and with a loading frequency of 4 Hz. Thousands of cycles of sinusoidal stress waves with a minimum deviator stress of 15 kPa and a maximum stress of 180kPa were applied during the cyclic loading period. Fig. 17 shows the simulation results and the corresponding experimental results. The decreasing cumulative axial strain with increasing confining pressure can be well captured by using $\alpha = 0.6$.

Figs 18 and 19 show the simulation results for monotonic and cyclic tests carried out by Fu et al. [43]. Monotonic tests were conducted on cylindrical specimens with a height of 700 mm and a diameter of 300 mm. Fig. 18 shows a comparison between the monotonic test results and corresponding model predictions, where good agreement can be observed. Cyclic tests were performed at two different load amplitudes of 1 MPa and 2 MPa with a constant loading frequency of 0.1 Hz. Fig. 19 shows the predicted results and the corresponding experimental data. An increase in the cumulative axial and volumetric strains with an increasing load amplitude is well captured by using $\alpha = 0.4$.

6 CONCLUSIONS

Fractional calculus is a powerful instrument for mathematically characterising and finding converging solutions to memory-intensive phenomena such as soil deformation. Although a few past studies have demonstrated the use of fractional calculus in quantifying the monotonic behaviour of different geomaterials, its adoption in predicting the true cyclic or dynamic behaviour of granular materials, as applicable for railways, has not been considered. In this study, it was shown that the strain accumulation rate of rail ballast obeyed a power law in relation to the number of loading cycles, and it could be described well using the concept of fractional calculus.

In essence, the major advantage of using fractional calculus in studying the cyclic behaviour of ballast was that it can extend traditional constitutive models developed for granular media (elastoplastic, generalised plasticity and bounding surface models) by using the fractional rate for strain accumulation.

By selecting the appropriate value of the fractional order, acceptable predictions of the strain accumulation rate with an increasing number of loading cycles could be obtained.

554 Accordingly, a simplified cyclic constitutive model for predicting the cumulative deformation
555 of ballast with increasing load cycles was developed by incorporating the fractional rate for
556 strain accumulation into a traditional bounding surface model. The model contains nine
557 parameters. Eight of them are inherited from the traditional plasticity models, with only one
558 additional parameter, the fractional order, specified for strain accumulation. All the
559 parameters can be easily obtained using triaxial tests. The proposed model simplifies to the
560 traditional plasticity model for monotonic loading when the fractional order is unity.

561 With the decrease of the fractional order (from 0.65 to 0.35), the model was observed to
562 exhibit faster cyclic densification under fully drained conditions. For instance, the strain
563 accumulation rate was decreased from 0.61% to 0.24% at N = 10 and from 0.12% to 0.03% at
564 N = 100. The proposed model was calibrated and validated against a series of independent
565 laboratory test results for ballast. It was found that the developed model can correctly
566 simulate the key features, such as stress-dilation under low confining pressure and strain-
567 hardening under relatively high confining pressure of ballast. For instance, at confining
568 pressures ranging from 10 kPa to 90 kPa, good predictions of the dilatation behaviour were
569 observed while volumetric contraction and strain hardening of the samples tested under
570 confining pressures ranging from 100 kPa to 400 kPa were also well simulated.

571 Simulations of the test results obtained under different cyclic loading conditions (e.g.,
572 different loading amplitudes, confining pressures, and loading frequencies) revealed that
573 unlike previous constitutive models for ballast, the current model can efficiently simulate the
574 cumulative deformation from the onset of loading to a large number of load cycles. For
575 instance, the cumulative axial, shear, and volumetric strains obtained under a variety of
576 confining pressures ranging from 20 kPa to 140 kPa were reasonably simulated by using
577 appropriate values of the fractional order (0.48 – 0.6). With the increase of confining pressure,
578 the cumulative axial strain decreased while the cumulative volumetric strain increased.
579 Cyclic densification of ballast under different loading frequencies (10 Hz – 40 Hz) can also
580 be captured by using a fractional order of 0.55.

581 The possible connection between fractional derivative order and fractal dimension was
582 only briefly discussed in the current study. However, further comprehensive studies could be
583 carried out through appropriate laboratory work or discrete element method in future, but is
584 not within the scope of this particular study. The fractional order was found to decrease with

585 the increasing fractal dimension of a given material. On the basis of this study, the fractional
586 order for ballast was found to be around 0.4 – 0.6.

587 Moreover, it should be noted that the current model was established on the basis of triaxial
588 test data to predict the cumulative deformation of ballast. The capability of this model to
589 evaluate limit loads or simulate more complex loading conditions, such as the rotation of
590 principal stress directions needs further experimental and numerical investigation which is
591 beyond the scope of this study.

592

593 ## ACKNOWLEDGEMENTS

594 The financial support provided by the China Scholarship Council [Grant No. 201306710022]
595 for the first author is greatly appreciated. This research is also supported by the Australian
596 Research Council through project expenses associated with the experimental work on rail
597 ballast.

598

599

APPENDIX

An attempt is made here to represent how the fractal dimension of the aggregates determines the fractional derivative order applicable during cyclic loading. To start with, the equation that considers energy dissipation due to particle breakage and the associated particle rearrangement in modified Cam-clay is adopted [47]:

$$p'\dot{\varepsilon}_v^p + q\dot{\varepsilon}_s^p = Mp'\dot{\varepsilon}_s^p + \frac{\Omega \dot{S}_s}{V_s(1+e_0)}(1+R) \tag{A1}$$

where $\dot{S}_s$ is the increment in surface area of particles within a sample, and Ω represents the surface energy. V_s is the soil volume. R is the ratio of energy dissipated by particle rearrangement to the energy dissipated by particle degradation. For simplicity of the analysis, R is assumed to be constant as also suggested by McDowell [48] and Nguyen and Einav [49]. A simple case for the isotropic compression condition is considered here, and accordingly, Eq. (A1) can be simplified as follows:

$$p'\dot{\varepsilon}_v^p = \frac{\Omega \dot{S}_s}{V_s(1+e_0)}(1+R) \tag{A2}$$

Fractal properties of a granular material under isotropic compression may now be combined with Eq. (A2) to derive the link between the fractional order and the fractal dimension of granular soils. While a material like ballast cannot be truly distributed in a fractal way because of the different origin and types of mineral particles and grain shapes, modelling the particle size distributions using fractals still provides a reasonable fit to experimental data [26, 50]. The number of particles with the diameter L, and larger than l_s obeys the following power law [25, 26]:

$$N_s(L > l_s) = A l_s^{-\Delta_s} \tag{A3}$$

where the subscript s denotes the solid. A is a constant of proportionality and Δ_s is the fractal dimension of the aggregates. Therefore, the incremental particle surface area can be obtained using Eq. (A3) as:

$$\dot{S}_s = \pi l_s^2 \gamma_s \dot{N}_s = A\Delta_s \gamma_s \pi l_s^{1-\Delta_s} \dot{l}_s \tag{A4}$$

where γ_s is the surface shape factor. Substituting Eq. (A4) into Eq. (A3) yields:

$$p'\dot{\varepsilon}_v^p = \frac{\Omega(1+R)}{V_s(1+e_0)} A\Delta_s \gamma_s \pi l_s^{1-\Delta_s} \dot{l}_s \tag{A5}$$

Eq. (A5) relates the stress-strain behaviour with the particle size, l_s, within the granular soil. The plastic deformation of granular soil is therefore attributed to the continuous degradation and redistribution of particles within the sample, as also indicated by McDowell and Bolton [47]. Suppose that the minimum particle size decreases by k times from the initial value for one loading cycle, then Eq. (A5) can be further expressed as:

$$\dot{\varepsilon}_v^p = \mu k^{\Delta_s - 3} \frac{\partial k}{\partial N} \tag{A6}$$

where μ is given by:

$$\mu = \frac{\Omega(1+R)}{V_s(1+e_0)p'} A\Delta_s \gamma_s \pi l_{s_0}^{2-\Delta_s} \tag{A7}$$

in which l_{s_0} denotes the initial minimum particle size within the sample, and the decreasing rate k changes with the number of load cycles. By recalling the relationship shown in Eq. (5) and using Eq. (3), an explicit expression for k can be obtained as:

$$k = \left[(\Delta_s - 2) N^{\alpha} / \alpha + 1 \right]^{1/(\Delta_s - 2)} \tag{A8}$$

A rapid increase followed by a stable variation of k with an increasing number of load cycles can be expected. The physical connection between the fractional derivative order and the fractal dimension can be further obtained using Eq. (A8) with N equal to 1, hence:

$$\alpha = (\Delta_s - 2)/(k_1^{\Delta_s - 2} - 1) \tag{A9}$$

where the parameter k_1 corresponds to the degradation rate of the minimum particle size at the first loading cycle. The fractional derivative order decreases as the fractal dimension of a given granular soil increases and approaches zero for a fractal dimension equal to 3, indicating that soils with higher fractal dimensions densify faster than those with lower fractal dimensions.

REFERENCES

[1] Carter JP, Booker JR, Wroth CP. A critical state soil model for cyclic loading. In: Pande GN, Zienkiewicz OC, editors. International Symposium on Soils Under Cyclic and Transient Loading. Swansea, Wales, United Kingdom: John Wiley & Sons Ltd, 1982. p. 219-52.

[2] Liu M, Carter JP. On the volumetric deformation of reconstituted soils. Int J Numer Anal Meth Geomech. 2000;24(2):101-33.

[3] Pastor M, Zienkiewicz OC, Chan AHC. Generalized plasticity and the modelling of soil behaviour. Int J Numer Anal Meth Geomech. 1990;14(3):151-90.

[4] Liu H, Zou D, Liu J. Constitutive modeling of dense gravelly soils subjected to cyclic loading. Int J Numer Anal Meth Geomech. 2014;38(14):1503-18.

[5] Khalili N, Habte M, Valliappan S. A bounding surface plasticity model for cyclic loading of granular soils. Int J Numer Meth Eng. 2005;63(14):1939-60.

[6] Österlöf R, Wentzel H, Kari L, Diercks N, Wollscheid D. Constitutive modelling of the amplitude and frequency dependency of filled elastomers utilizing a modified Boundary Surface Model. Int JSolids Struct. 2014;51(19):3431-8.

[7] Xiao Y, Liu H, Chen Y, Jiang J. Bounding surface model for rockfill materials dependent on density and pressure under triaxial stress conditions. J Eng Mech. 2014;140(4):04014002.

[8] Xiao Y, Liu H, Chen Y, Jiang J. Bounding surface plasticity model incorporating the state pressure index for rockfill materials. J Eng Mech. 2014;140(11):04014087.

[9] Chen Q, Indraratna B, Carter J, Nimbalkar S. An Isotropic-Kinematic Hardening Model for Coarse Granular Soils Capturing Particle Breakage and Cyclic Loading under Triaxial Stress Space. Canadian Geotechnical Journal. 2015.

[10] Lekarp F, Dawson A. Modelling permanent deformation behaviour of unbound granular materials. Construct Build Mater. 1998;12(1):9-18.

[11] Kargah-Ostadi N, Stoffels S. Framework for Development and Comprehensive Comparison of Empirical Pavement Performance Models. J Transport Eng. 2015;141(8):04015012.

[12] Suiker ASJ, de Borst R. A numerical model for the cyclic deterioration of railway tracks. Int J Numer Meth Eng. 2003;57(4):441-70.

[13] François S, Karg C, Haegeman W, Degrande G. A numerical model for foundation settlements due to deformation accumulation in granular soils under repeated small amplitude dynamic loading. Int J Numer Anal Meth Geomech. 2010;34(3):273-96.

[14] Indraratna B, Thakur PK, Vinod JS, Salim W. Semiempirical Cyclic Densification Model for Ballast Incorporating Particle Breakage. Int J Geomech. 2012;12(3):260-71.

[15] López-Querol S, Coop MR. Drained cyclic behaviour of loose Dogs Bay sand. Géotechnique. 2012;62(4):281-9.

[16] Koeller RC. Applications of fractional calculus to the theory of viscoelasticity. J Appl Mech. 1984;51(2):299-307.

[17] Sun Y, Liu H, Xiao Y, Gao H, Cui Y. Modeling of rheological behavior of geomaterials based on fractional viscoelastic equation with variable parameters. In: Louis Ge XZ, Antnio Gomes Correia, Jason Wu, editor. GeoHunan International Conference 2011. Hunan, China: ASCE, 2011. p. 107-14.

[18] Yin D, Duan X, Zhou X. Fractional time-dependent deformation component models for characterizing viscoelastic Poisson's ratio. Europ J Mech A Solids. 2013;42(422-9.

[19] Yin D, Wu H, Cheng C, Chen Y. Fractional order constitutive model of geomaterials under the condition of triaxial test. Int J Numer Anal Meth Geomech. 2013;37(8):961-72.

[20] Fenander A. Frequency dependent stiffness and damping of railpads. Proceed Inst Mech Eng. 1997;211(1):51-62.

[21] Sun H, Chen W, Chen Y. Variable-order fractional differential operators in anomalous diffusion modeling. Physica A: Statistical Mechanics and its Applications. 2009;388(21):4586-92.
[22] Chen W, Sun H, Zhang X, Korošak D. Anomalous diffusion modeling by fractal and fractional derivatives. Comput Math Appl. 2010;59(5):1754-8.
[23] Podlubny I. Fractional differential equations: an introduction to fractional derivatives, fractional differential equations, to methods of their solution and some of their applications. San Diego, California: Academic press, 1998.
[24] Xu Y, Xia X. Fractal model for virgin compression of pure clays. Mech Res Commun. 2006;33(2):206-16.
[25] Russell AR. A compression line for soils with evolving particle and pore size distributions due to particle crushing. Geotech Lett. 2011;1(1):5-9.
[26] McDowell GR, De Bono JP, Yue P, Yu HS. Micro mechanics of isotropic normal compression. Geotech Lett. 2013;3(4):166-72.
[27] Meng R, Yin D, Zhou C, Wu H. Fractional description of time-dependent mechanical property evolution in materials with strain softening behavior. Appl Math Model. 2016;40(1):398-406.
[28] Sun Y, Indraratna B, Nimbalkar S. Three-dimensional characterisation of particle size and shape for ballast. Geotech Lett. 2014;4(3):197-202.
[29] Indraratna B, Sun Y, Nimbalkar S. Laboratory assessment of the role of particle size distribution on the deformation and degradation of ballast under cyclic loading. J Geotech Geoenviron Eng. 2016;142(7):04016016.
[30] ASTM. Standard test method for consolidated undrained triaxial compression test for cohesive soils. West Conshohocken, PA, USA: ASTM International, 2011.
[31] Wichtmann T, Rondón H, Niemunis A, Triantafyllidis T, Lizcano A. Prediction of Permanent Deformations in Pavements Using a High-Cycle Accumulation Model. J Geotech Geoenviron Eng. 2010;136(5):728-40.
[32] Aursudkij B, McDowell GR, Collop AC. Cyclic loading of railway ballast under triaxial conditions and in a railway test facility. Granular Matter. 2009;11(6):391-401.
[33] Sevi A, Ge L. Cyclic behaviors of railroad ballast within the parallel gradation scaling framework. J Mater Civil Eng. 2012;24(7):797-804.
[34] Schofield A, Wroth P. Critical state soil mechanics. New York, USA: McGraw-Hill London, 1968.
[35] Li X, Dafalias Y. Dilatancy for cohesionless soils. Géotechnique. 2000;50(4):449-60.
[36] Ling HI, Yang S. Unified sand model based on the critical state and generalized plasticity. J Eng Mech. 2006;132(12):1380-91.
[37] Salim W, Indraratna B. A new elastoplastic constitutive model for coarse granular aggregates incorporating particle breakage. Can Geotech J. 2004;41(4):657-71.
[38] Indraratna B, Sun QD, Nimbalkar S. Observed and predicted behaviour of rail ballast under monotonic loading capturing particle breakage. Canadian Geotechnical Journal. 2014;52(1):73-86.
[39] Dafalias YF. Bounding surface plasticity. I: Mathematical foundation and hypoplasticity. Journal of engineering mechanics. 1986;112(9):966-87.
[40] Bardet J. Bounding surface plasticity model for sands. J Eng Mech. 1986;112(11):1198-217.
[41] Russell AR, Khalili N. A bounding surface plasticity model for sands exhibiting particle crushing. Can Geotech J. 2004;41(6):1179-92.
[42] Kan M, Taiebat H, Khalili N. Simplified mapping rule for bounding surface simulation of complex loading paths in granular materials. Int J Geomech. 2014;14(2):239-53.

746 [43] Fu Z, Chen S, Peng C. Modeling cyclic behavior of rockfill materials in a framework of
747 generalized plasticity. Int J Geomech. 2014;14(2):191-204.
748 [44] Khalili N, Habte M, Zargarbashi S. A fully coupled flow deformation model for cyclic
749 analysis of unsaturated soils including hydraulic and mechanical hystereses. Comput Geotech.
750 2008;35(6):872-89.
751 [45] Anderson WF, Fair P. Behavior of railroad ballast under monotonic and cyclic loading. J
752 Geotech Geoenviron Eng. 2008;134(3):316-27.
753 [46] Sun Q, Indraratna B, Nimbalkar S. Deformation and Degradation Mechanisms of
754 Railway Ballast under High Frequency Cyclic Loading. J Geotech Geoenviron Eng.
755 2015;142(1):04015056.
756 [47] McDowell GR, Bolton MD. On the micromechanics of crushable aggregates.
757 Géotechnique. 1998;48(5):667-79.
758 [48] McDowell G. A family of yield loci based on micro mechanics. Soils and foundations.
759 2000;40(6):133-7.
760 [49] Nguyen GD, Einav I. The Energetics of Cataclasis Based on Breakage Mechanics. Pure
761 Appl Geophys. 2009;166(1693-724.
762 [50] Coop M, Sorensen K, Freitas TB, Georgoutsos G. Particle breakage during shearing of a
763 carbonate sand. Géotechnique. 2004;54(3):157-63.

764

Table caption list:

Table 1 Material properties and test conditions

Table 2 Model parameters

770 Table 1. Material properties and test conditions

Materials	Test ID	e_0	q_{min} (kPa)	q_{max} (kPa)	C_u	d_M (mm)	d_{60} (mm)	d_{50} (mm)	d_{30} (mm)	d_{10} (mm)	d_m (mm)
Current study	S100	0.686	-	-	1.9	45	43.7	34.6	33.7	19. 5	9.5
		0.735									
	S200	0.653									
		0.728									
	S400	0.620									
		0.711									
	C30f20	0.713	45	230							
		0.688									
	C60f20	0.708									
		0.655									
	C120f20	0.671									
		0.623									
Anderson & Fair [45]	S40	0.838	-	-	1.4	50	42.3	40.2	35.7	30	14
	S90	0.812									
	C90f0.5	0.730	15	250							
	C140f0.5	0.720									
Aursudkij et al. [32]	S10	0.721	-	-	1.5	50	41.7	39.4	34.5	27.4	22.4
	S30	0.689									
	S60	0.683									
	C30f4	0.668	15	180							
	C60f4	0.655									
Fu et al., [43]	S08	0.199	-	-	63	10	3.6	2.6	0.9	0.06	-
	S2	0.199									
	S3	0.199									
	C3f0.1	0.199	3500	5500							
			2500	6500							
Indraratna et al. [14]	C60f10	0.720	45	230	1.5	53	41.0	38.3	32.9	26.5	19
	C60f20	0.720									
	C60f40	0.720									
Salim & Indraratna [37]	S100	0.682	-	-	1.5	53	40.2	37	31.7	26.8	19
	S200	0.653									
	S300	0.627									
Sevi & Ge [33]	C20f1	0.690	0	88,121	1.6	19	12.0	11.1	9.3	7.7	2.8
	C20f1	0.690	0	102,121		38	23.9	22.2	18.5	15.4	5.6
Sun et al. [46]	C30f10	0.720	45	230	1.5	53	41.1	39.5	34.2	26.8	16
	C60f10	0.720									

771 Table 2. Model parameters

Data sources	Test series	κ	ν	ϕ_{cr}	λ	e_{Γ}	γ	a	c	α
Current study	Monotonic	0.009	0.3	46.5	0.234	2.137	1.0	2	0	1.0
	Cyclic	0.009	0.3	46.5	0.234	2.137	1.0	0.429	0.850	0.5
Salim & Indraratna [37]	Monotonic	0.007	0.3	45.7	0.188	1.830	1.0	1.65	0	1.0
Indraratna et al. [14]	Cyclic	0.007	0.3	55.0	0.188	1.830	7.0	232.55	-0.835	0.55
Sun et al. [46]	Cyclic	0.007	0.3	53.0	0.182	1.830	1.8	0.543	1.383	0.53
Anderson & Fair [45]	Monotonic	0.001	0.3	43.0	0.180	1.840	1.0	0.427	0.855	1.0
	Cyclic	0.001	0.3	43.0	0.180	1.840	1.0	0.104	1.835	0.48
Aursudkij et al. [32]	Monotonic	0.002	0.3	42.6	0.068	1.182	1.0	0.5	0	1.0
	Cyclic	0.002	0.3	42.6	0.068	1.182	0.4	0.122	1.415	0.6
Fu et al. [43]	Monotonic	0.008	0.3	41.0	0.160	1.840	1.0	0.249	-0.831	1.0
	Cyclic	0.008	0.3	41.0	0.160	1.840	0.8	20	-0.415	0.4

Figure caption list:

Fig. 1. Axial strain accumulation rate vs number of load cycles for ballast in (a) log-linear scale and (b) log-log scale

Fig. 2. Volumetric strain accumulation rate vs number of load cycles for ballast in (a) log-linear scale and (b) log-log scale

Fig. 3. Strain accumulation rate vs number of load cycles for ballast [33]: (a) volumetric strain rate (b) axial strain rate

Fig. 4. Position of the initial bounding surface

Fig.5. Flow chart for model implementation

Fig. 6. Schematic representation of the effect of the fractional order on soil densification: (a) stress-strain response and (b) accumulated strain vs number of load cycles

Fig. 7. Model simulation for drained compression tests on medium dense ballast (R_d = 0.56 – 0.63)

Fig. 8. Model predictions of (a) axial strain and (b) volumetric strain of medium dense (R_d = 0.56 – 0.63) ballast under different confining pressures

Fig. 9. Model simulation for drained compression tests on dense ballast (R_d = 0.70 – 0.89)

Fig. 10. Model predictions of (a) axial strain and (b) volumetric strain of dense (R_d = 0.70 – 0.89) ballast under different confining pressures

Fig. 11. Model simulation for drained compression tests on ballast (data sourced from [37])

Fig. 12. Model predictions of (a) shear strain and (b) volumetric strain of ballast (data sourced from [14]) under different load frequencies

Fig. 13. Model predictions of (a) shear strain and (b) volumetric strain of ballast (data sourced from [46]) under different confining pressures

Fig. 14. Model predictions of (a) axial strain vs deviator stress and (b) axial strain vs volumetric strain of ballast (data sourced from [45])

797 Fig. 15. Model predictions of (a) shear strain and (b) volumetric strain of ballast under
798 different confining pressures (data sourced from [45])

799 Fig. 16. Model predictions of (a) axial strain vs deviator stress and (b) axial strain vs
800 volumetric strain of ballast (data sourced from [32])

801 Fig. 17. Model predictions of (a) axial strain and (b) volumetric strain of ballast under
802 different confining pressures (data sourced from [32])

803 Fig. 18. Model predictions of (a) axial strain vs deviator stress and (b) axial strain vs
804 volumetric strain (data sourced from [43])

805 Fig. 19. Model predictions of (a) axial strain and (b) volumetric strain under different loading
806 amplitudes (data sourced from [43])

807

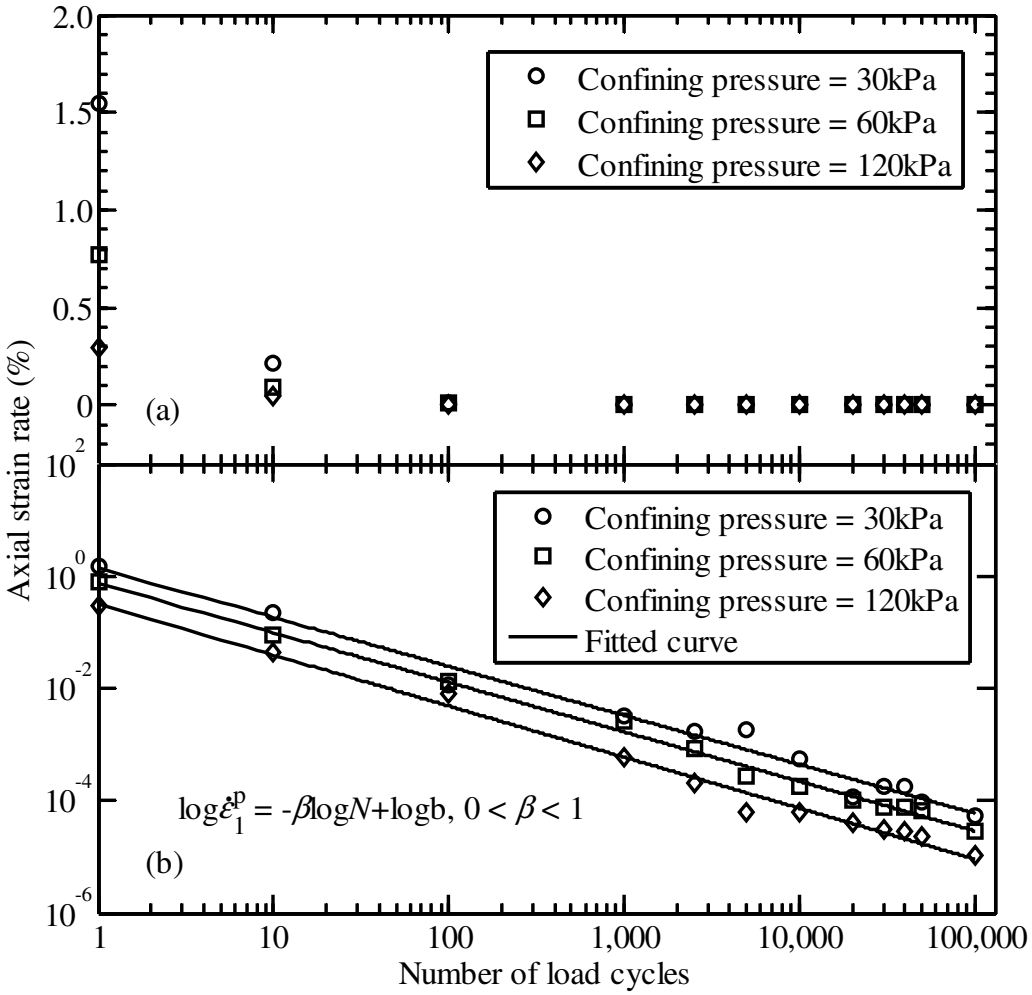

Fig. 1. Axial strain accumulation rate vs number of load cycles for ballast in (a) log-linear scale and (b) log-log scale

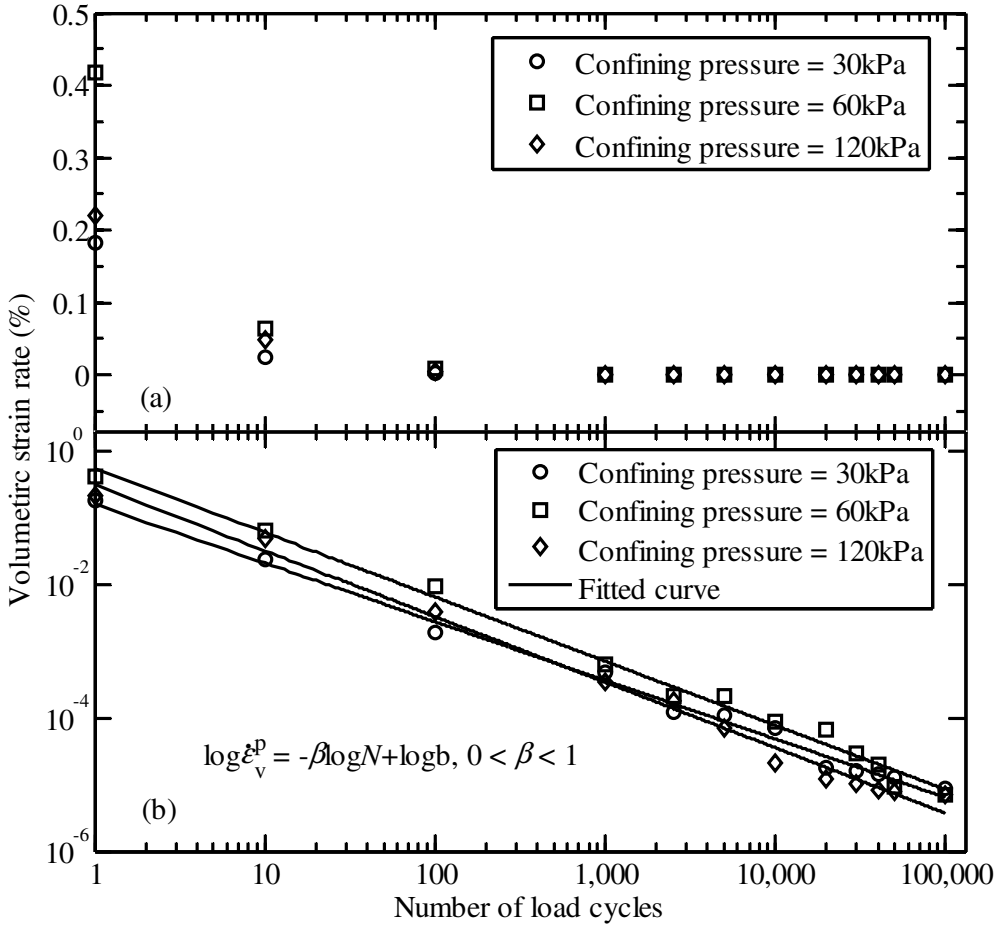

Fig. 2. Volumetric strain accumulation rate vs number of load cycles for ballast in (a) log-linear scale and (b) log-log scale

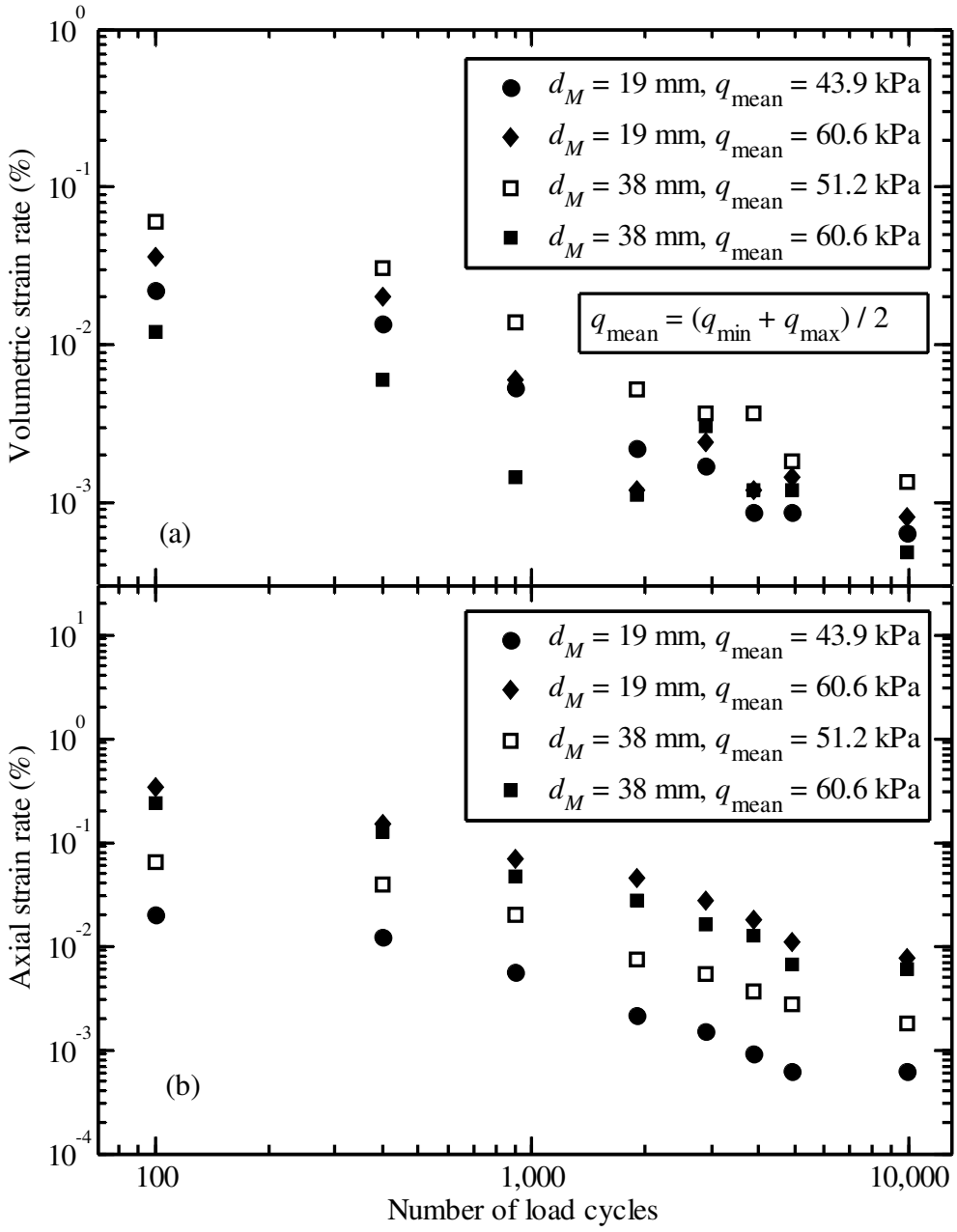

816

817 Fig. 3. Strain accumulation rate vs number of load cycles for ballast [33]: (a) volumetric
818 strain rate (b) axial strain rate

819

820

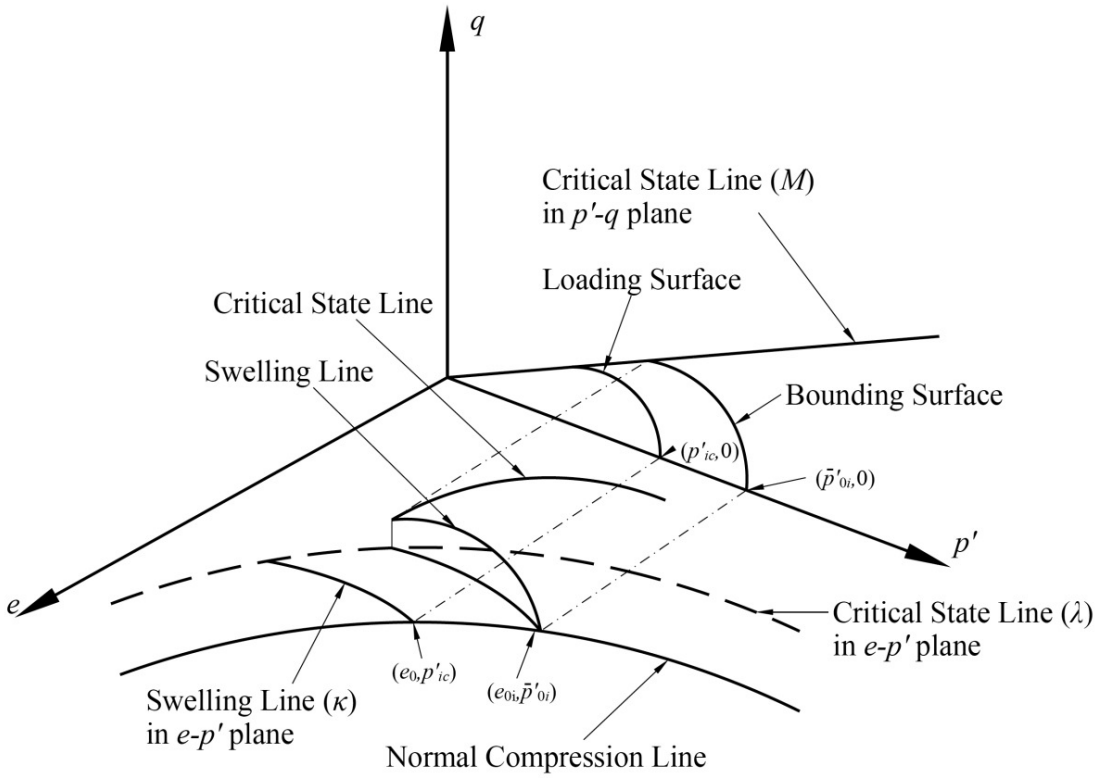

821

822 Fig. 4. Position of the initial bounding surface

823

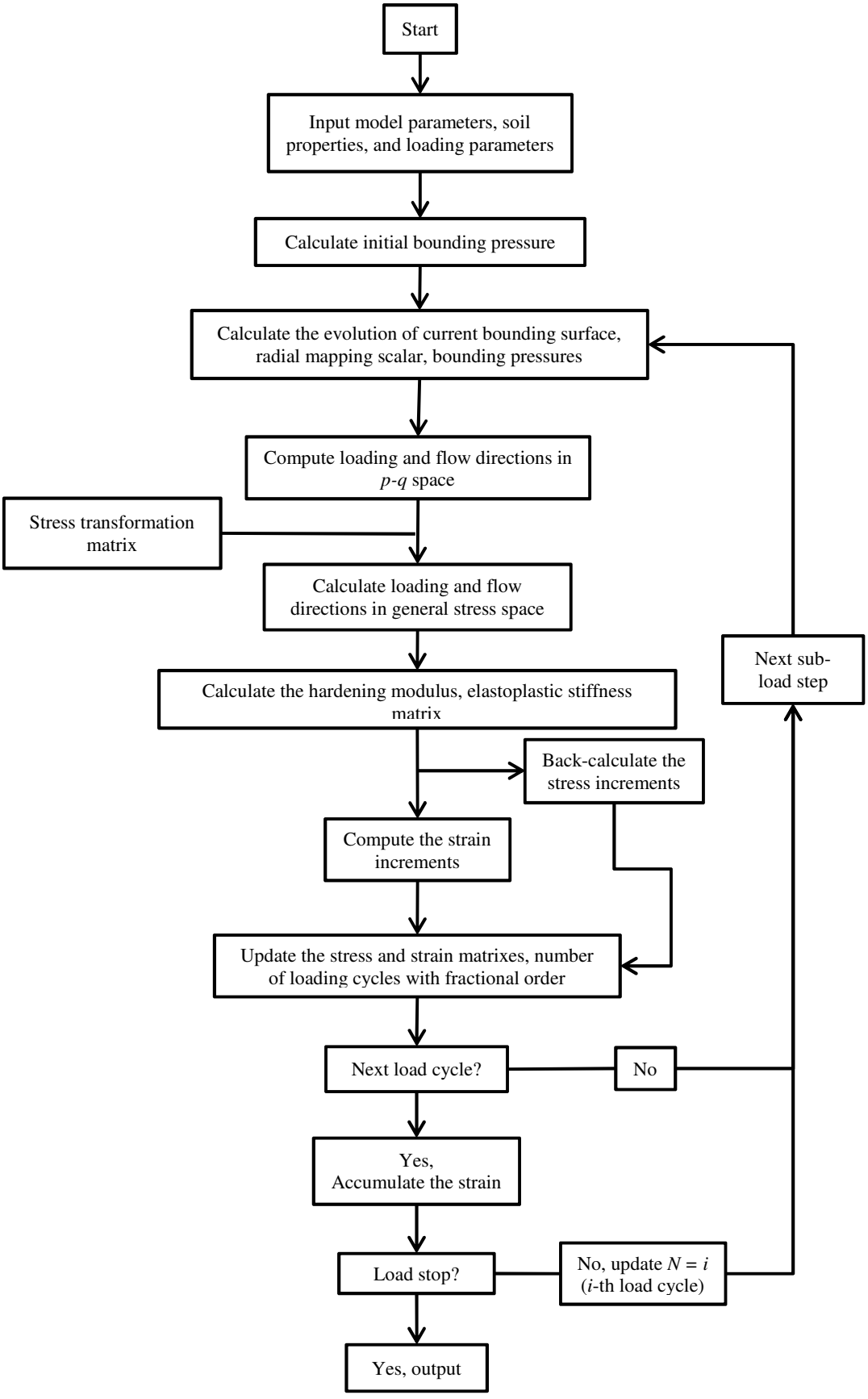

824

825 Fig.5 Flow chart for model implementation

826

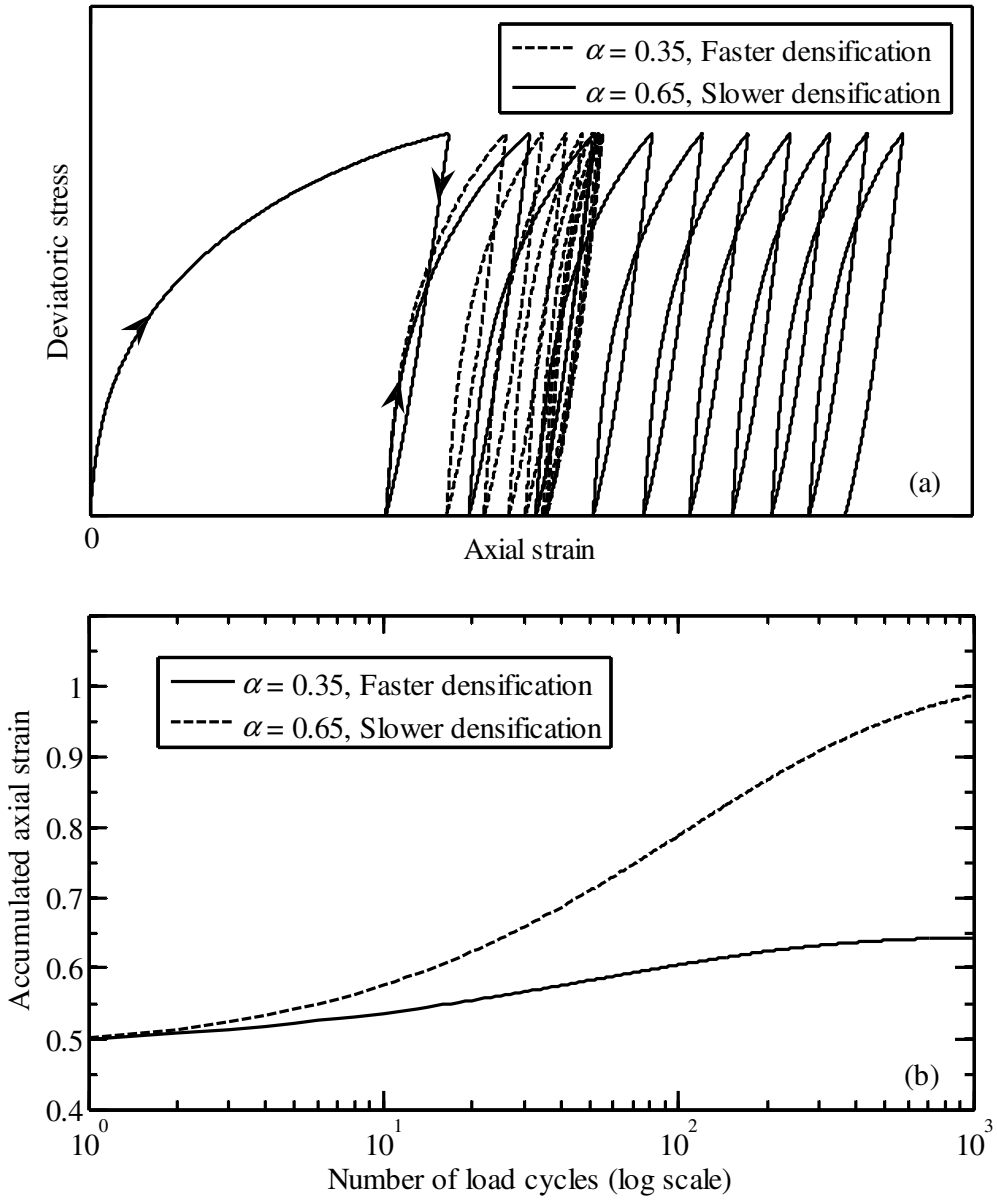

827

828 Fig. 6. Schematic representation of the effect of the fractional order on soil densification: (a)
829 stress-strain response and (b) accumulated strain vs number of load cycles

830

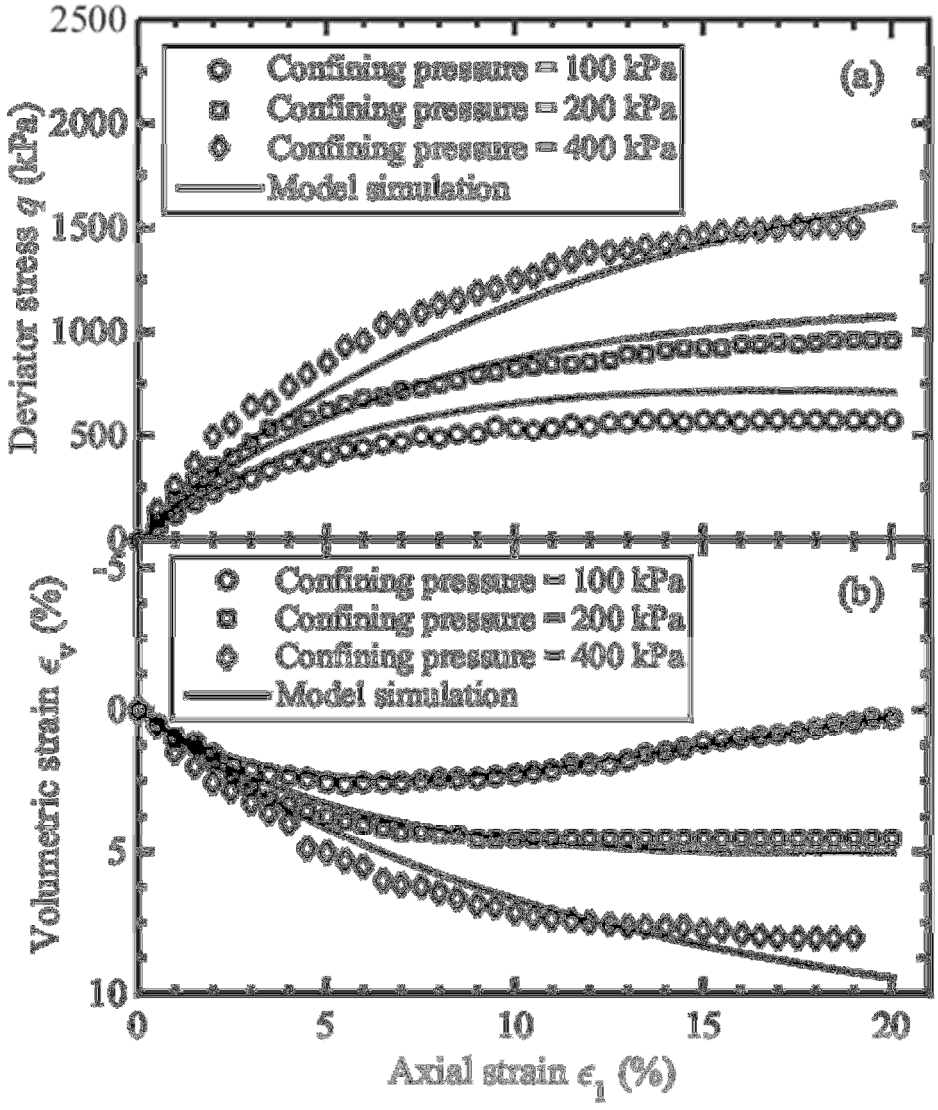

831

832 Fig. 7. Model simulation for drained compression tests on medium dense ballast (R_d = 0.56 –

833 0.63)

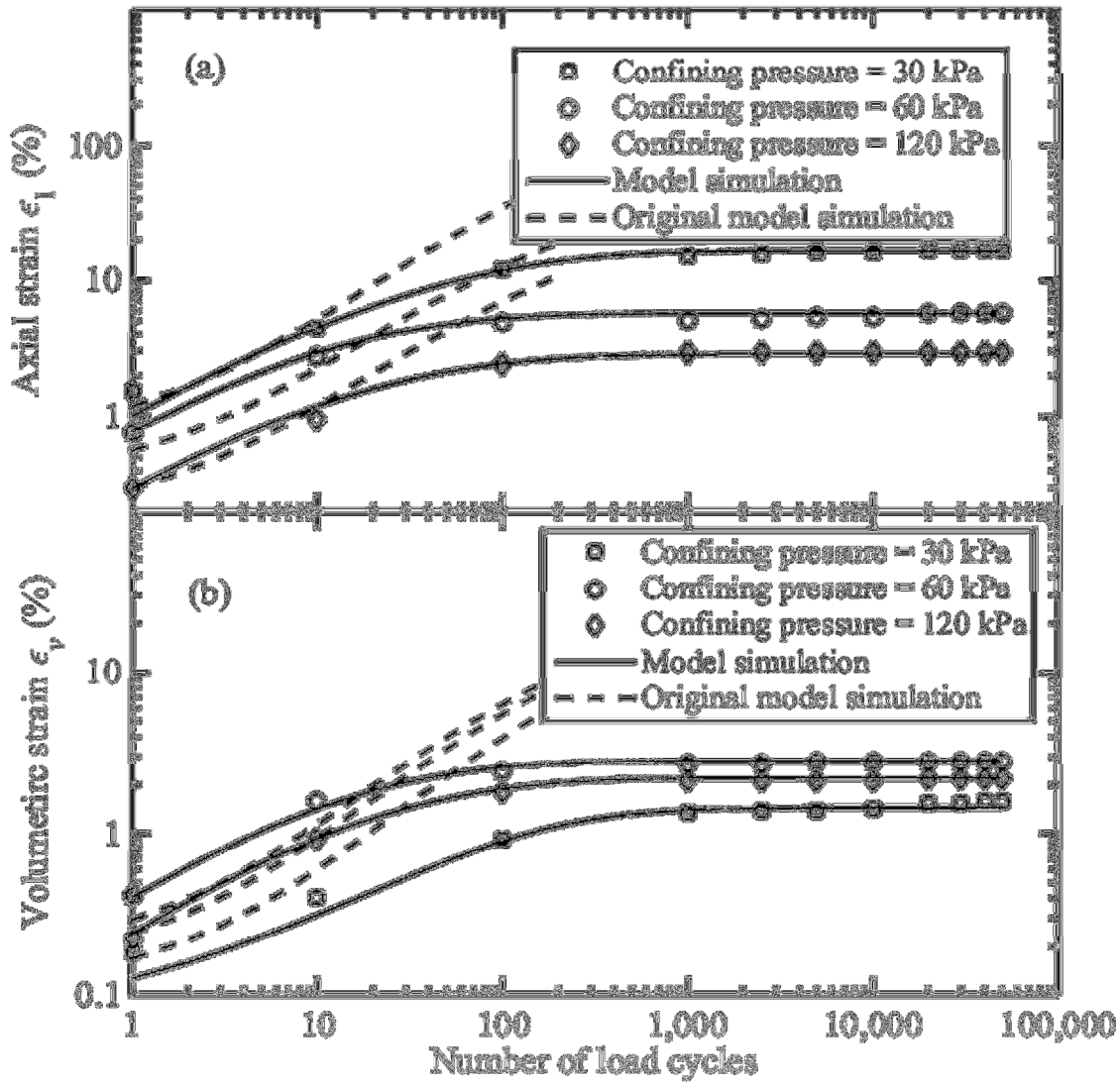

834

835 Fig. 8. Model predictions of (a) axial strain and (b) volumetric strain of medium dense (R_d =
836 0.56 – 0.63) ballast under different confining pressures

837

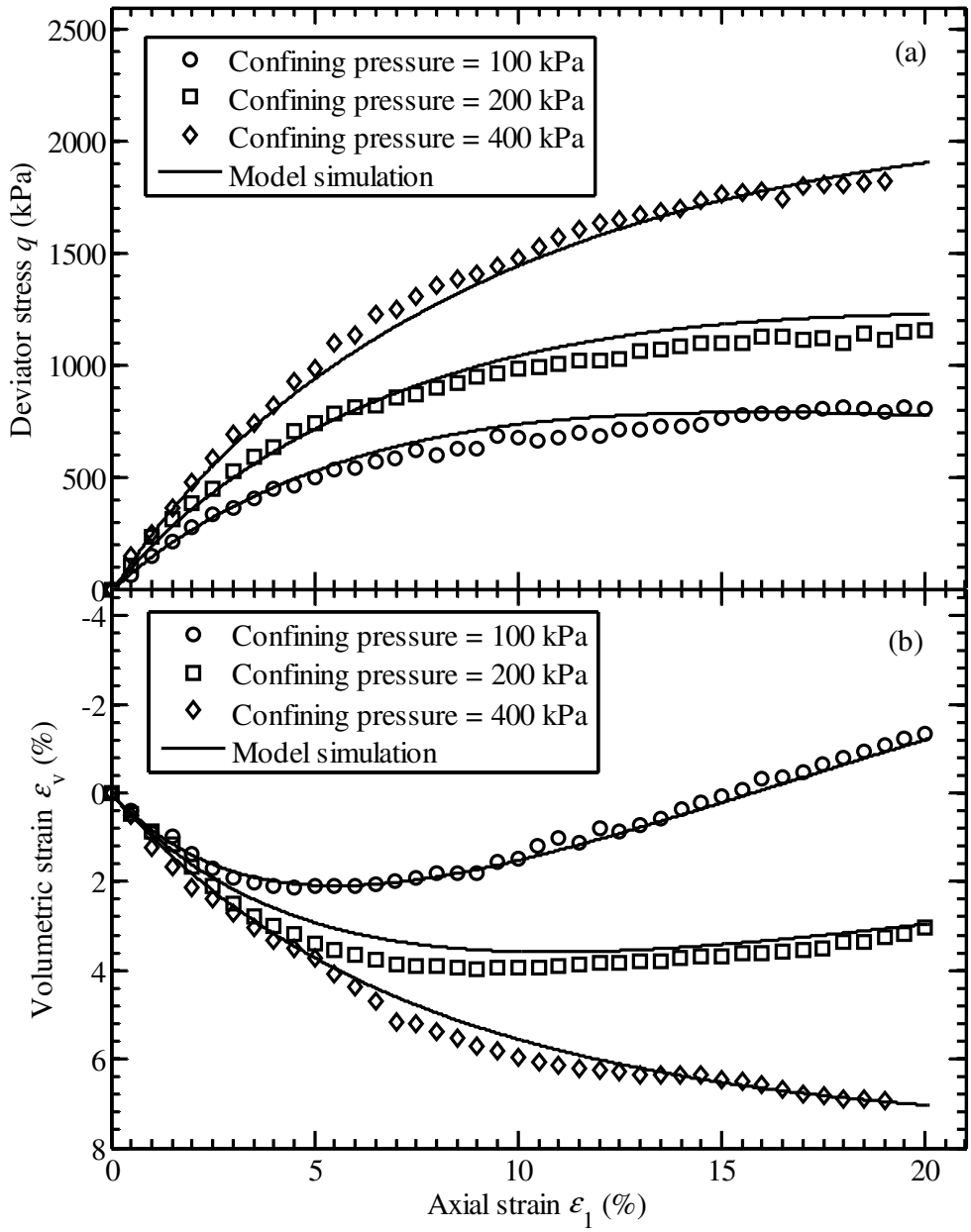

838

839 Fig. 9. Model simulation for drained compression tests on dense ballast (R_d = 0.70 – 0.89)

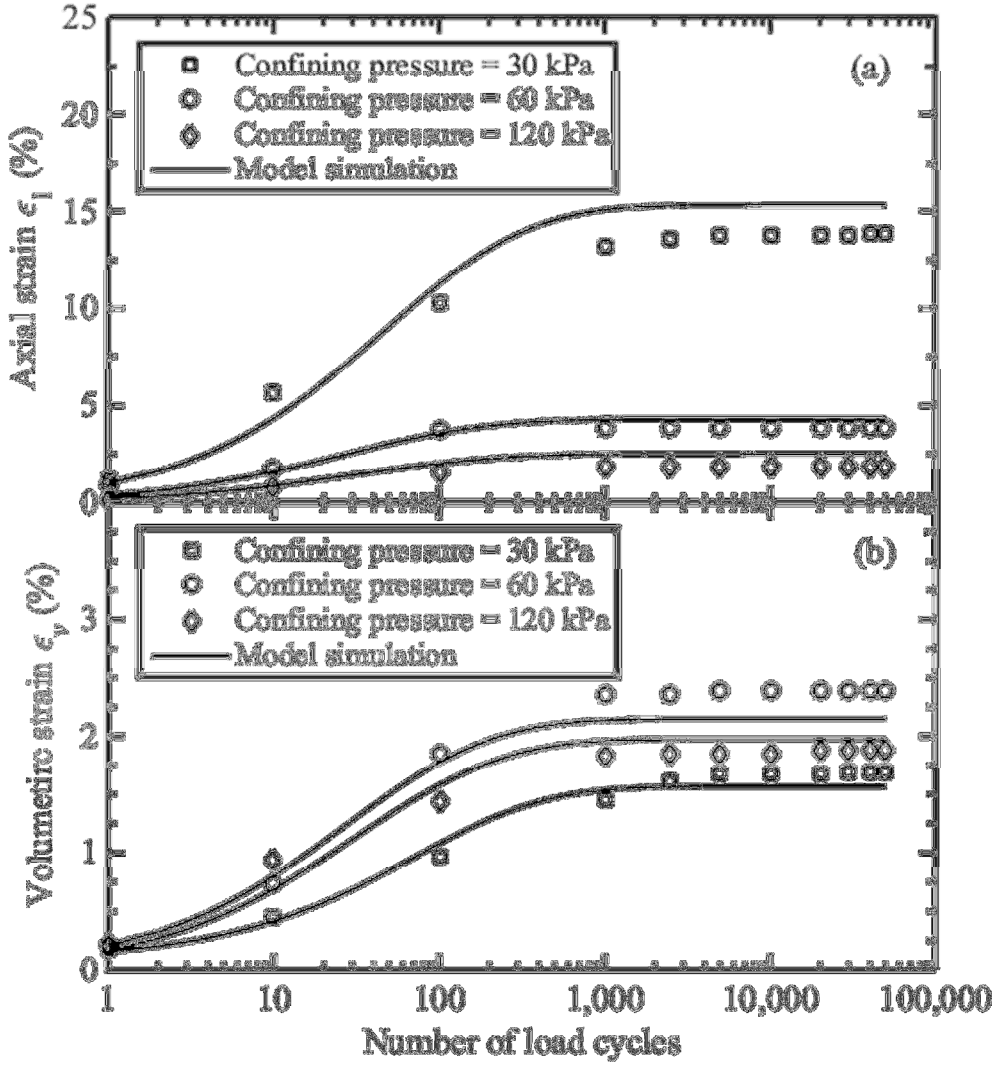

840

841 Fig. 10. Model predictions of (a) axial strain and (b) volumetric strain of dense (R_d = 0.70 –

842 0.89) ballast under different confining pressures

843

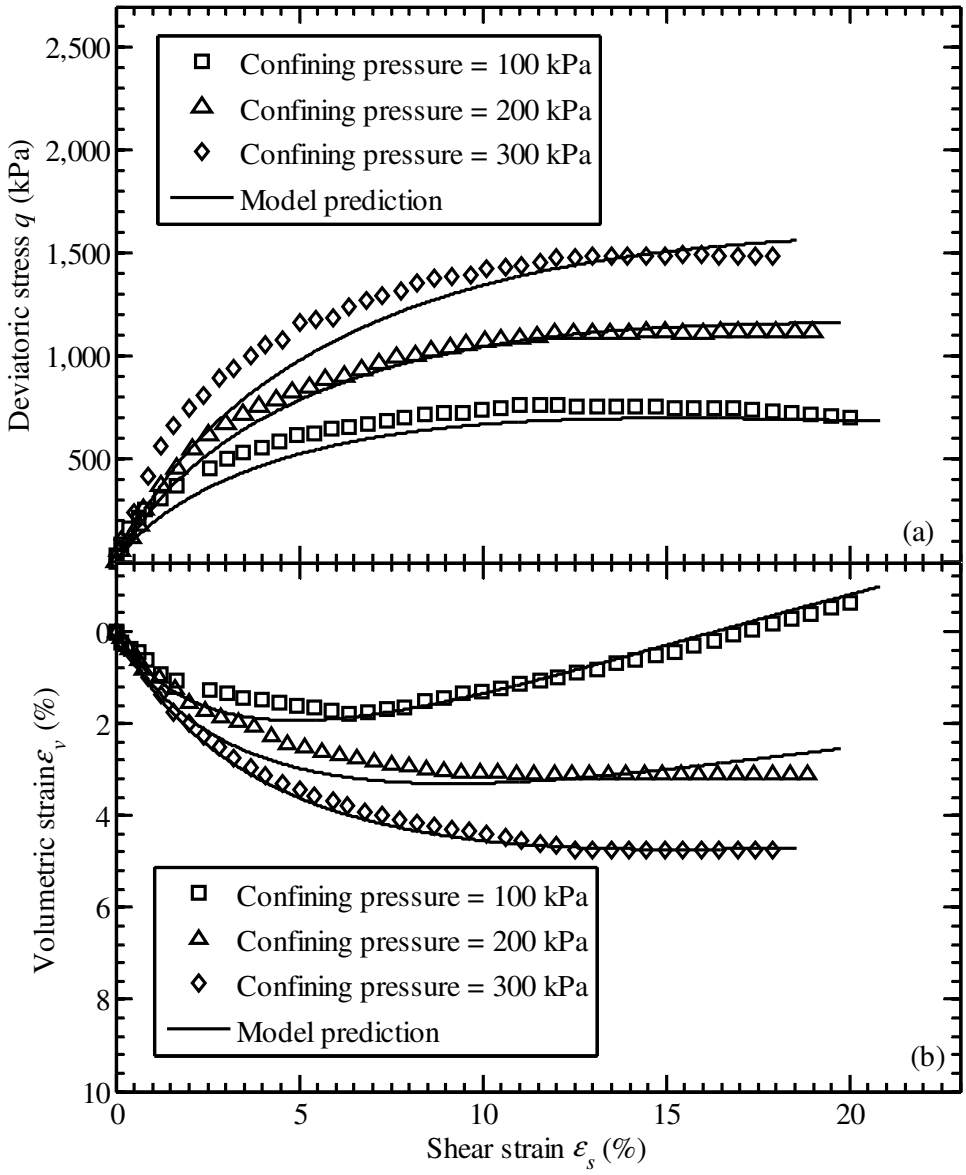

844

845 Fig. 11. Model simulation for drained compression tests on ballast (data sourced from Salim
846 and Indraratna [37])

847

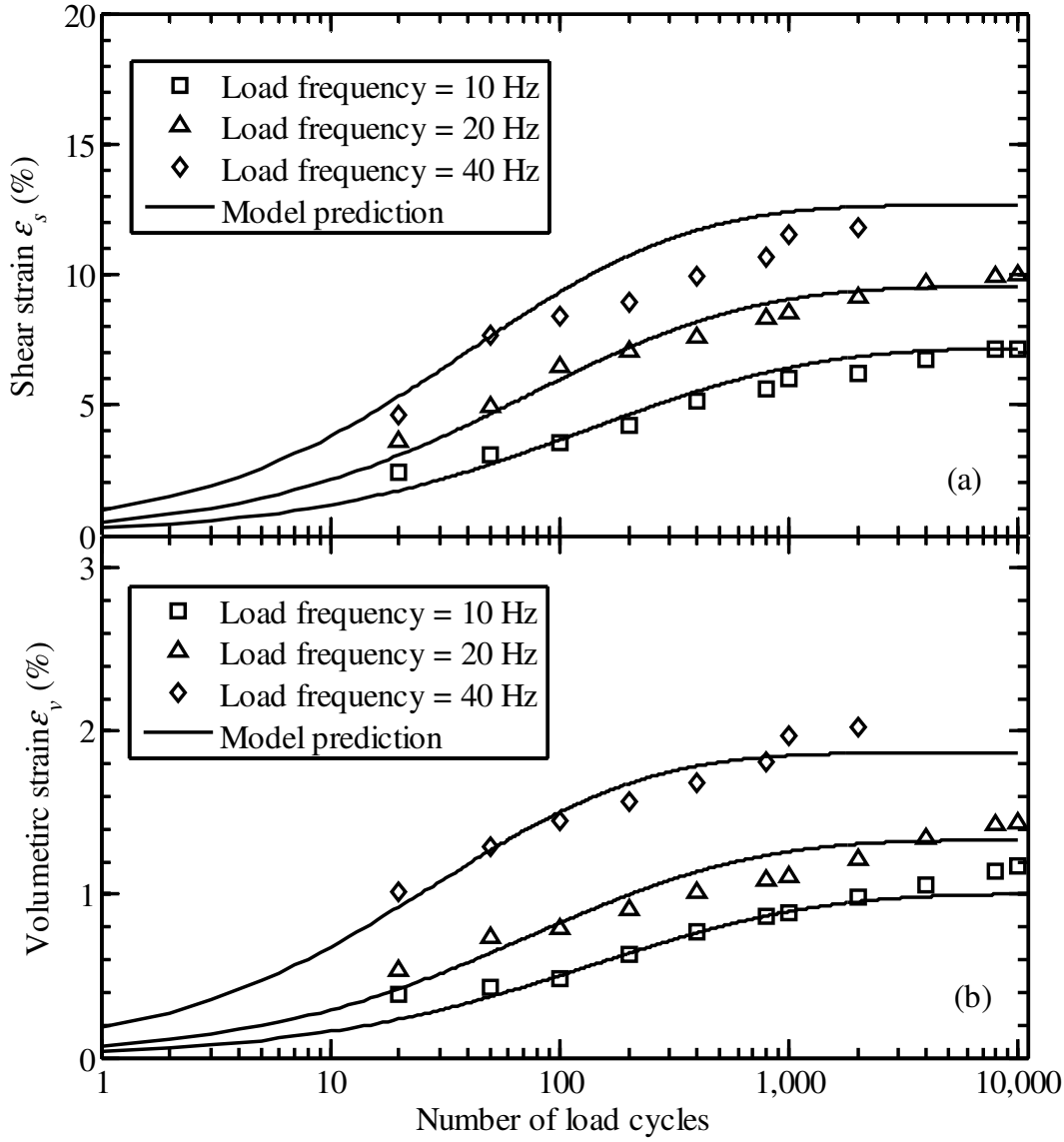

Fig. 12. Model predictions of (a) shear strain and (b) volumetric strain of ballast (data sourced from [14]) under different load frequencies

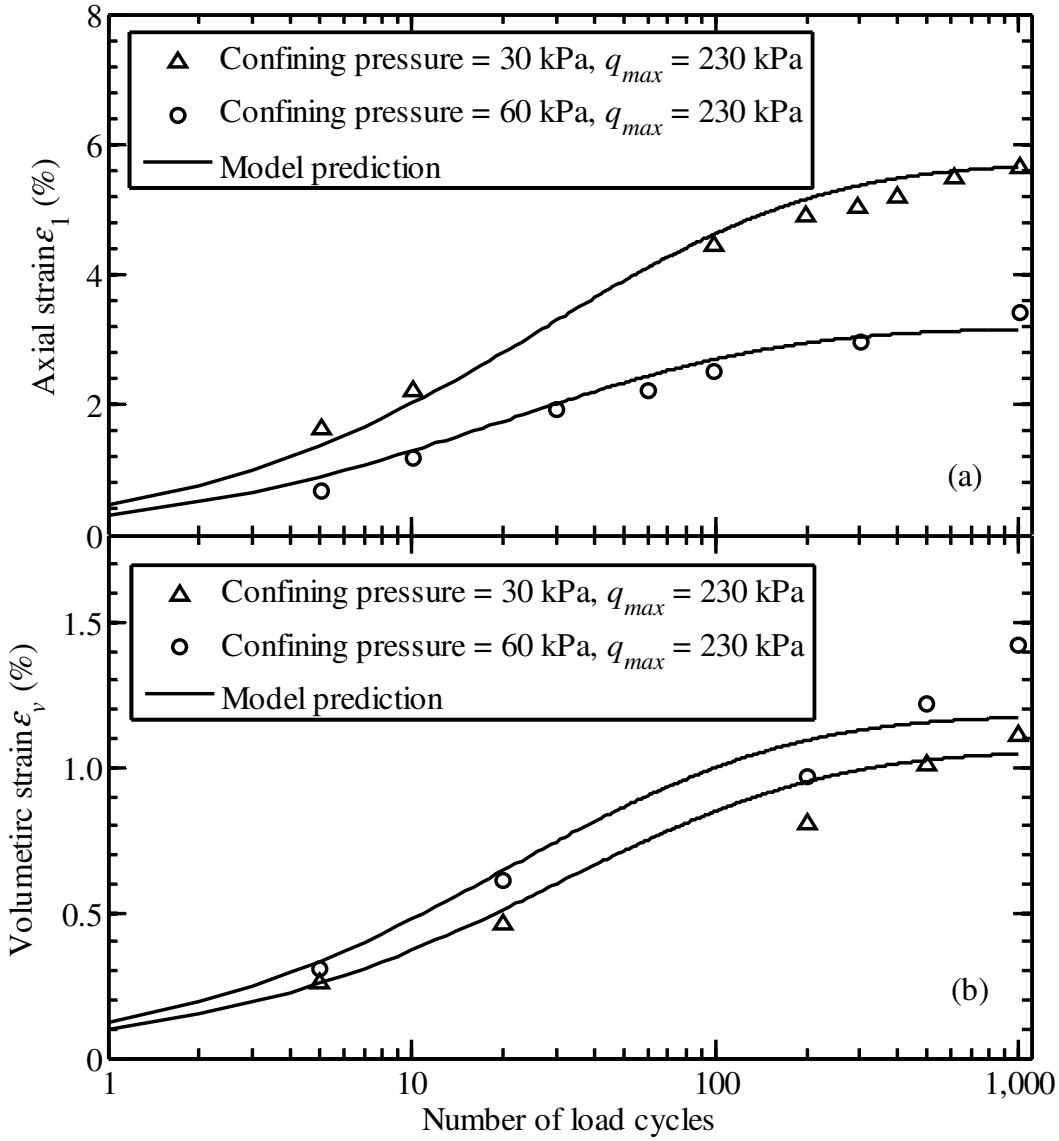

Fig. 13. Model predictions of (a) axial strain and (b) volumetric strain of ballast (data sourced from [46]) under different confining pressures

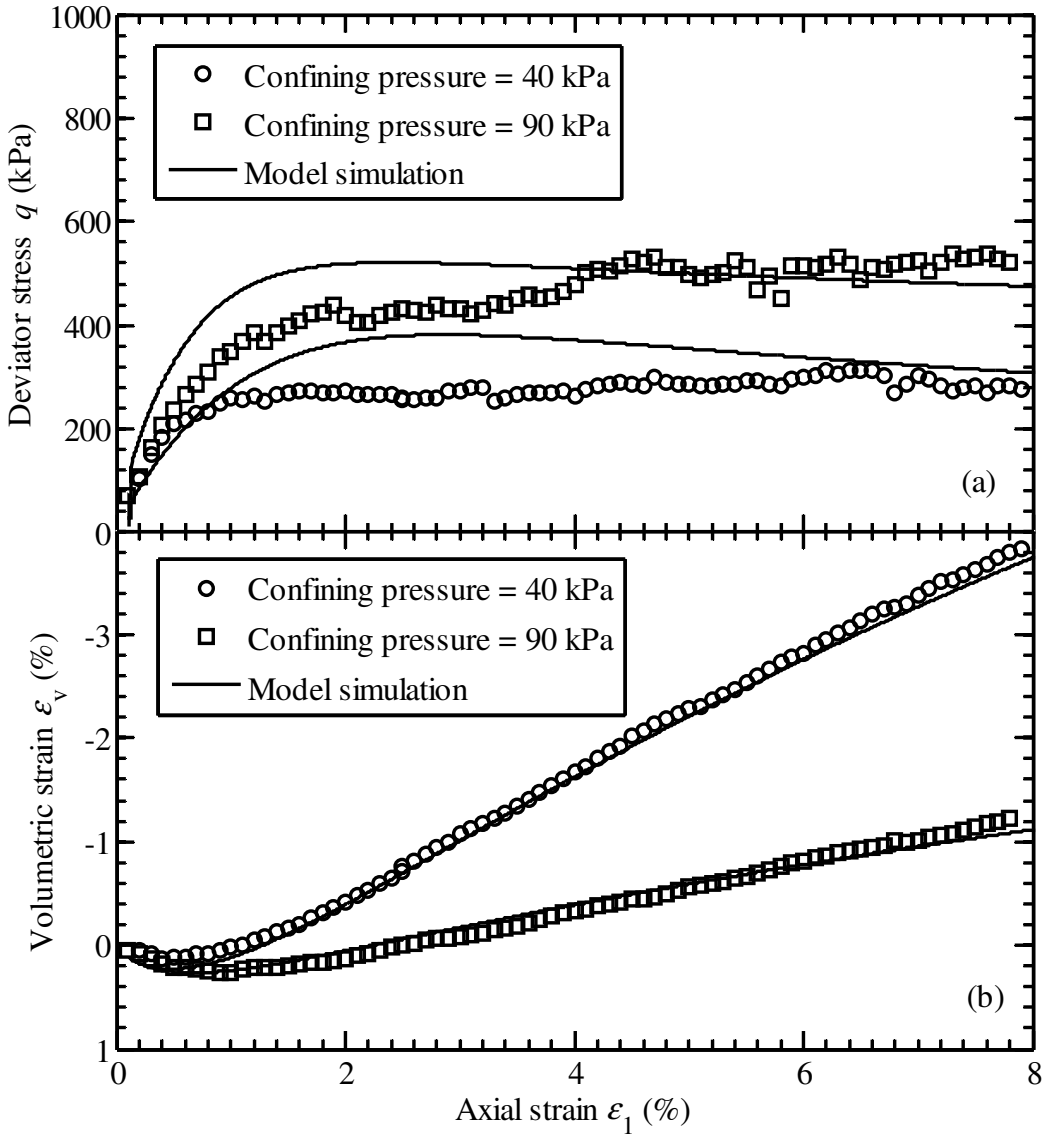

854

855 Fig. 14. Model predictions of (a) axial strain vs deviator stress and (b) axial strain vs
856 volumetric strain of ballast (data sourced from [45])

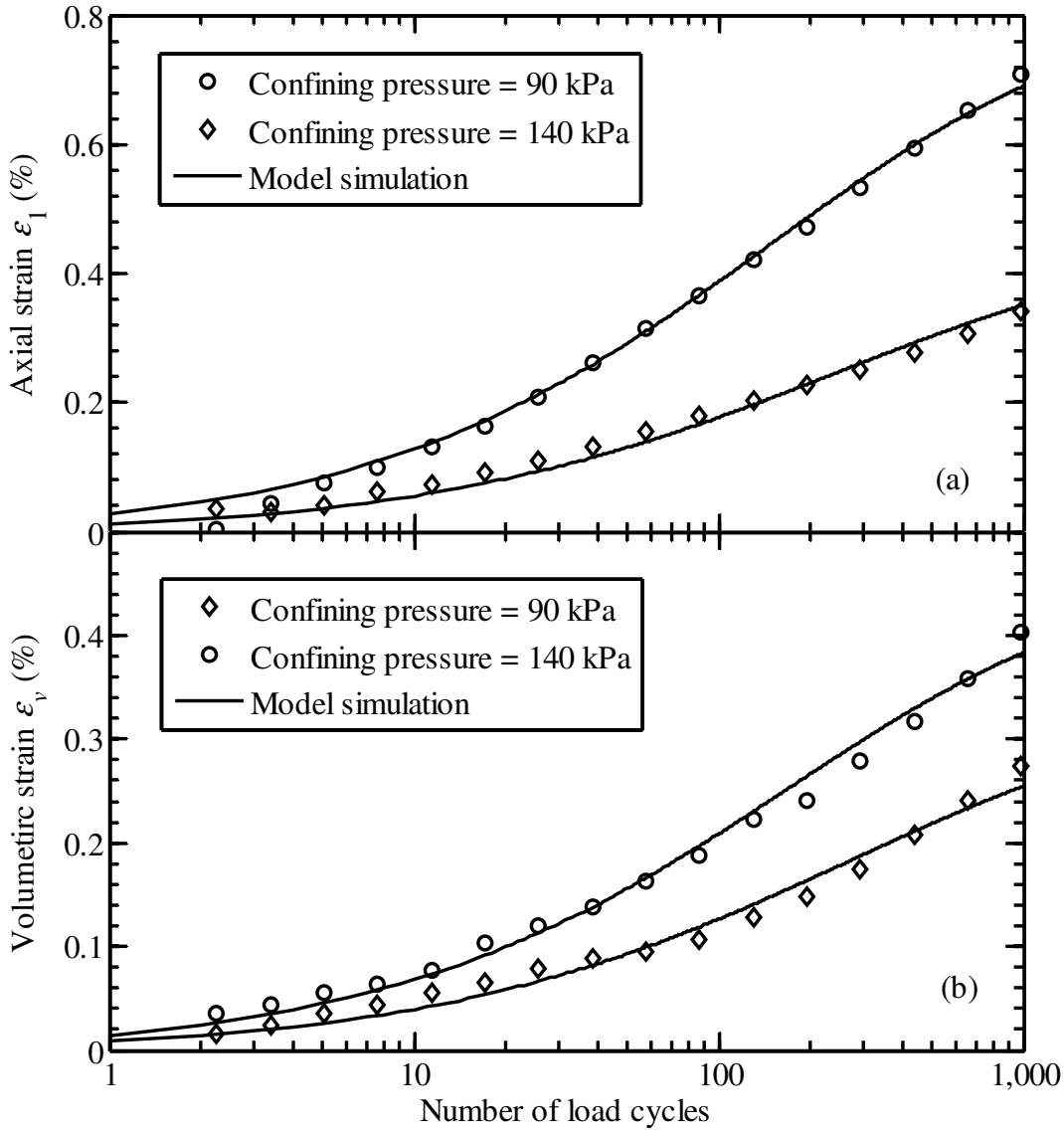

857

858 Fig. 15. Model predictions of (a) axial strain and (b) volumetric strain of ballast under
859 different confining pressures (data sourced from [45])

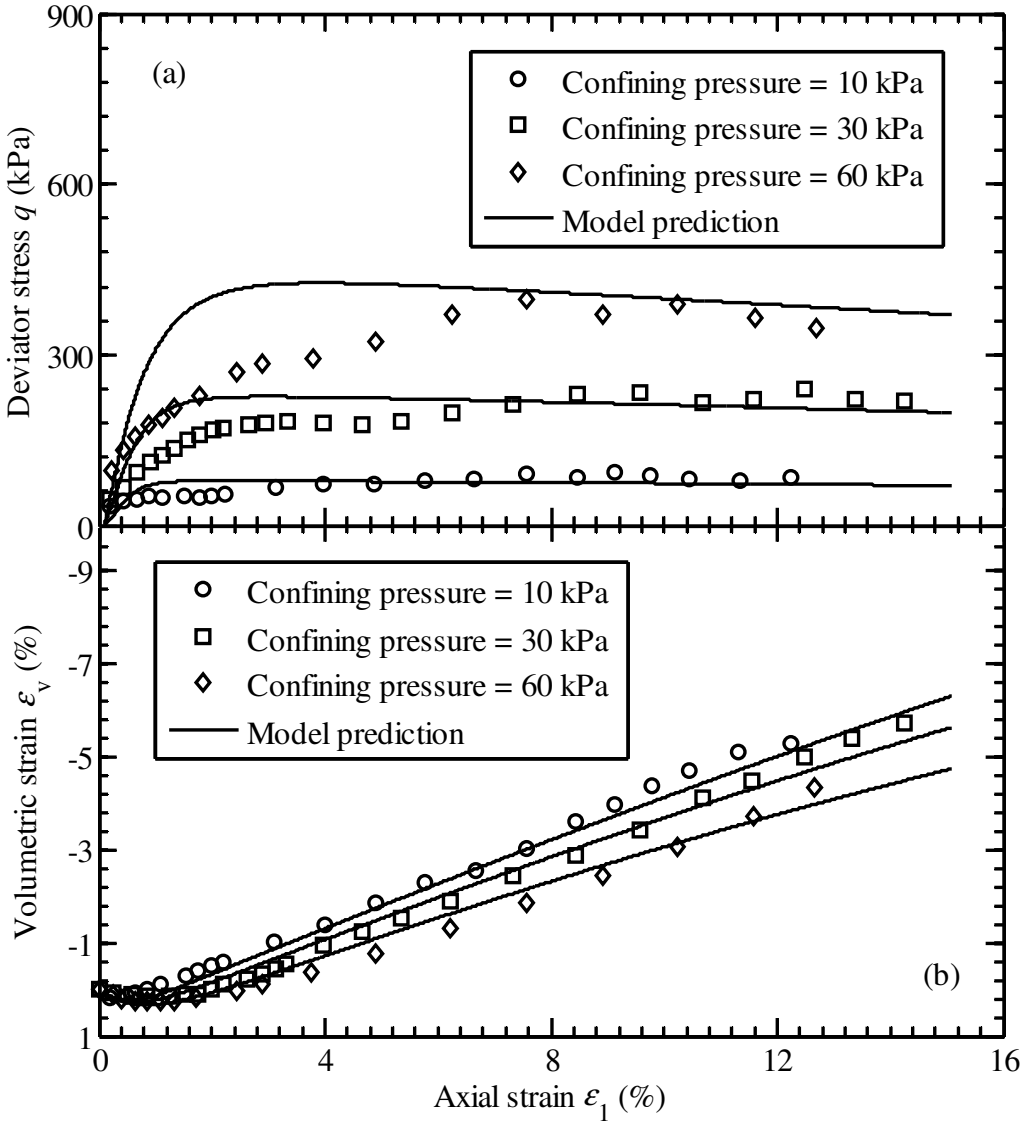

860

861 Fig. 16. Model predictions of (a) axial strain vs deviator stress and (b) axial strain vs

862 volumetric strain of ballast (data sourced from [32])

863

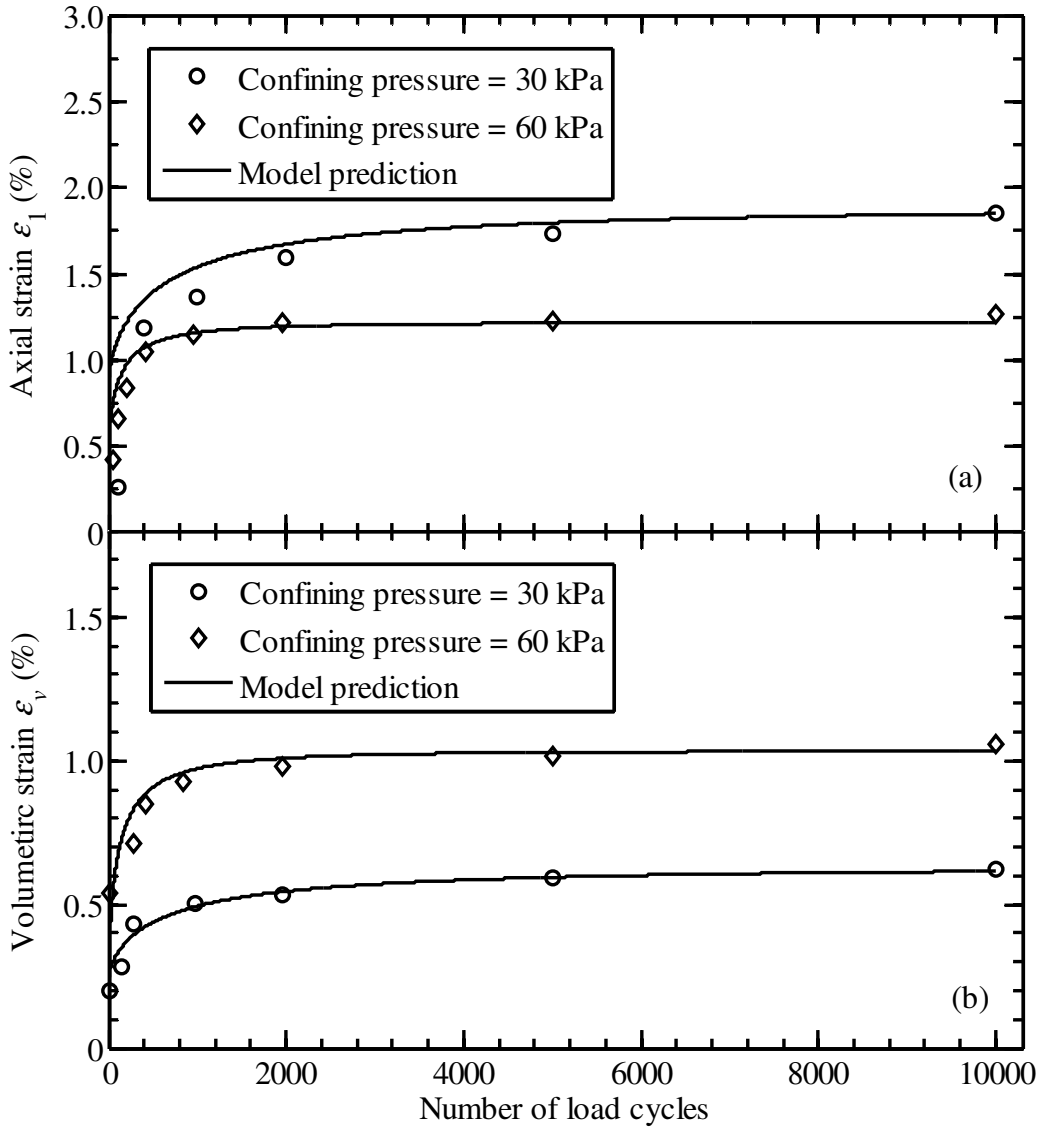

Fig. 17. Model predictions of (a) axial strain and (b) volumetric strain of ballast under different confining pressures (data sourced from [32])

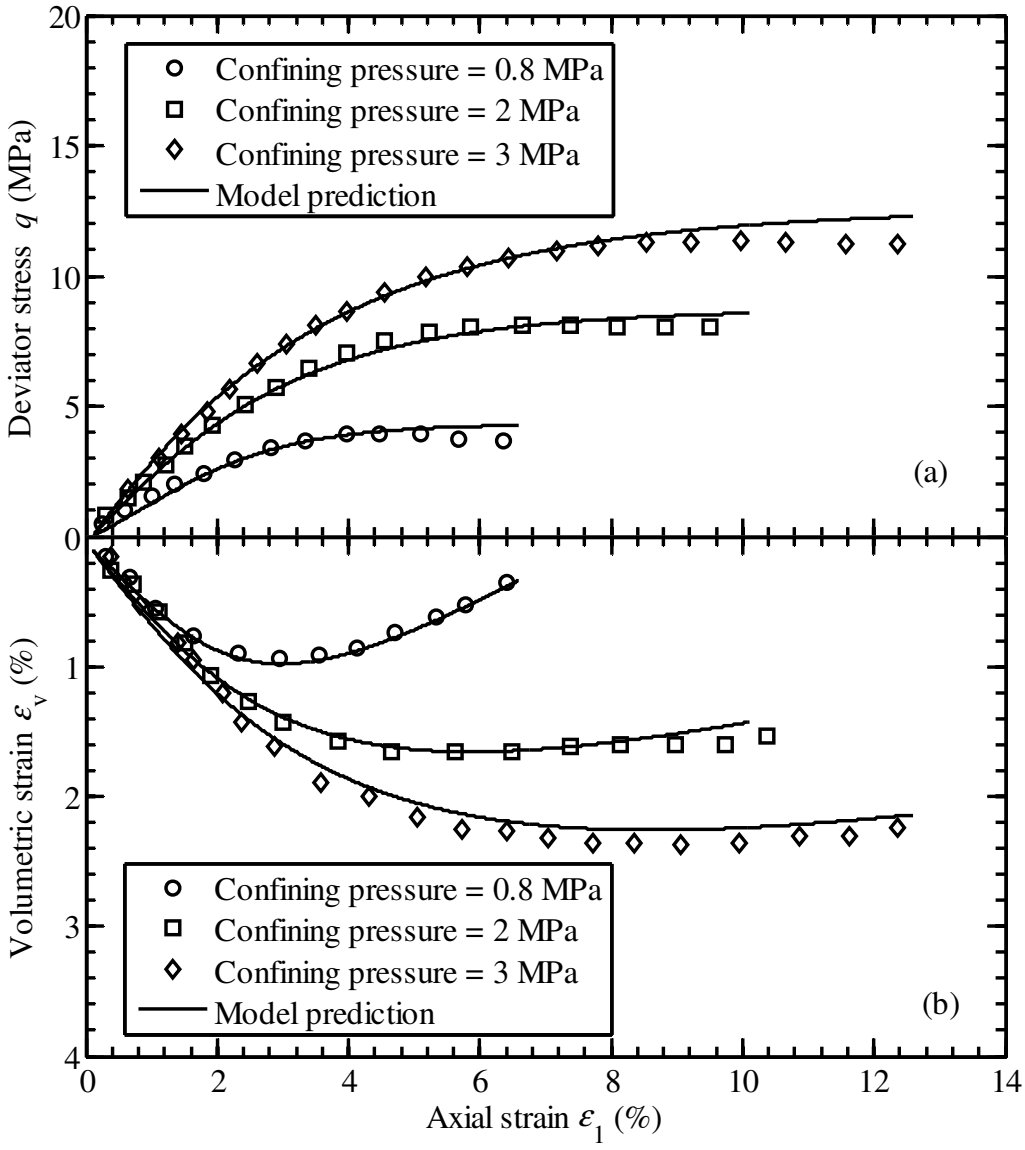

869

870 Fig. 18. Model predictions of (a) axial strain vs deviator stress and (b) axial strain vs
871 volumetric strain (data sourced from [43])

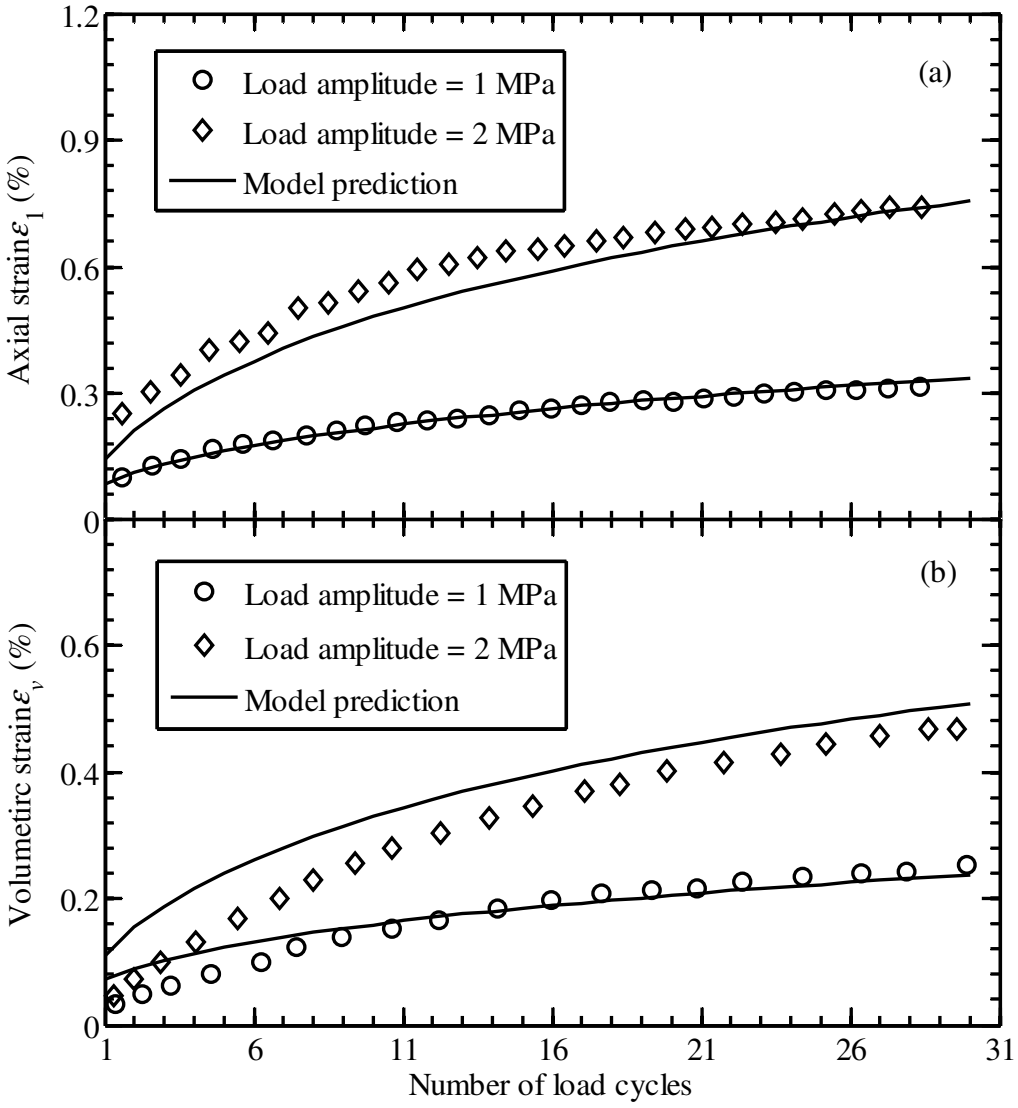

872

873 Fig. 19. Model predictions of (a) axial strain and (b) volumetric strain under different loading
874 amplitudes (data sourced from [43])

875